

# The chemodynamical memory of a major merger in a NIHAO-UHD<sup>★</sup> Milky Way analogue I: A golden thread through time and space

Sven Buder,<sup>1</sup> †‡ Tobías Buck,<sup>2,3</sup> Ása Skúladóttir,<sup>4</sup> Melissa Ness,<sup>1</sup> Madeleine McKenzie,<sup>5</sup> § and Stephanie Monty<sup>6,7</sup>

<sup>1</sup>Research School of Astronomy and Astrophysics, Australian National University, Canberra, ACT 2611, Australia

<sup>2</sup>Universität Heidelberg, Interdisziplinäres Zentrum für Wissenschaftliches Rechnen, Im Neuenheimer Feld 205, D-69120 Heidelberg, Germany

<sup>3</sup>Universität Heidelberg, Zentrum für Astronomie, Institut für Theoretische Astrophysik, Albert-Ueberle-Straße 2, D-69120 Heidelberg, Germany

<sup>4</sup>Dipartimento di Fisica e Astronomia, Università degli Studi di Firenze, Via G. Sansone 1, I-50019 Sesto Fiorentino, Italy

<sup>5</sup>The Observatories of the Carnegie Institution for Science, 813 Santa Barbara Street, Pasadena, 91101, CA, USA

<sup>6</sup>Institute of Astronomy, University of Cambridge, Madingley Road, Cambridge CB3 0HA, UK

<sup>7</sup>Department of Astronomy, New Mexico State University, Las Cruces, NM 88003, USA

Accepted DD MM 2025. Received DD MM 2025; in original form DD MM 2025

## ABSTRACT

Understanding how the Milky Way’s present-day structure was shaped by past major mergers is a key goal of Galactic archaeology. The chemical and dynamical structure of the Galaxy retains the imprint of such events, including a major accretion episode around 8–10 Gyr ago. Recent findings suggest that present-day orbital energy correlates with stellar chemistry and birth location within the merging progenitor galaxy. Using a high-resolution NIHAO-UHD cosmological zoom-in simulation of a Milky Way analogue, we trace the birth positions, ages, and present-day orbits of stars accreted in its last major merger. We show that stars born in the progenitor’s core are more tightly bound to the Milky Way and chemically enriched, while those from the outskirts are less bound and metal-poor. This supports the scenario proposed by Skúladóttir et al. (2025) using idealised simulations, now demonstrated in a cosmological context. The preserved chemodynamical memory is also evident in elemental planes such as [Al/Fe] vs. [Mg/Mn], reflecting gradients in star formation efficiency. The median abundance trends for different orbital energies are broadly similar, though less pronounced and more non-linear than the linear relations reported by Skúladóttir et al. (2025), with relatively good agreement at the highest metallicities. Our results reveal that spatial and temporal memory is retained across the merger – connecting birth locations to present-day properties like a golden thread. We demonstrate that selection methods in integrals-of-motion space systematically bias progenitor reconstructions by missing its enriched core, and we outline strategies to obtain a more representative census of accreted stars.

**Key words:** Galaxy: evolution – Galaxy: formation – Galaxy: structure – Galaxy: abundances – Galaxy: kinematics and dynamics

## 1 INTRODUCTION

Understanding what shaped the Milky Way and its present-day structure remains a central goal of Galactic archaeology (Freeman & Bland-Hawthorn 2002; Bland-Hawthorn & Gerhard 2016). The discovery of the thin and thick stellar disc components (Yoshii 1982; Gilmore & Reid 1983), characterised by their largely distinct spatial, chemical and age distributions (for example Bensby et al. 2014; Hayden et al. 2015), has led to numerous formation scenarios being proposed. These include turbulent high-redshift star formation producing a kinematically hot thick disc (Bird et al. 2013; Stinson et al. 2013), internal heating and radial migration within an evolving disc (Schöenrich & Binney 2009; Minchev et al. 2013; Sharma et al.

2021), a strong sensitivity of star formation to temporarily lower gas accretion (Grand et al. 2018; Orkney et al. 2025), as well as gas-rich mergers (Brook et al. 2004; Buck 2020) and the build-up of the disc under a two-infall scenario (Chiappini et al. 1997; Spitoni et al. 2019). More and more likely it seems to actually be a combination of multiple pathways (e.g. Orkney et al. 2025).

Thanks to new observations of the *Gaia* satellite (Brown 2021) and spectroscopic follow-up it has become evident that the Milky Way’s halo is built from numerous substructures, providing clear signatures of both past and ongoing accretion events (Belokurov et al. 2006; Myeong et al. 2018; Koppelman et al. 2019; Naidu et al. 2020; Yuan et al. 2020; Dodd et al. 2023). One particularly influential finding is that a major merger (hereafter called *GSE*) with an estimated mass ratio between 1:2.5 and 1:4 (Helmi et al. 2018; Naidu et al. 2020) occurred roughly 8–10 billion years ago, somewhat disrupting the protodisc and certainly contributing significantly to the halo. Early hints of this event came from stellar abundance patterns (Nissen & Schuster 2010), and were later confirmed with significant dynamical information from the *Gaia* mission (Gaia Collaboration et al. 2016,

\* NIHAO-UHD is the Ultra High Definition re-run of a Milky Way analogue from the *Numerical Investigation of a Hundred Astronomical Objects* (NIHAO) suite (Wang et al. 2015).

† E-mail: sven.buder@anu.edu.au

‡ Australian Research Council DECRA Fellow

§ NASA Hubble Fellow

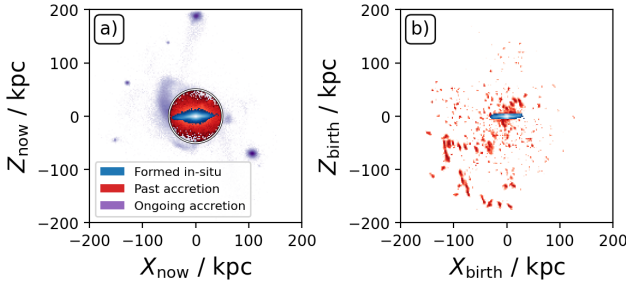


**Figure 1.** Tracing in-situ stars (blue) alongside past (red) and ongoing (purple) accretion components, shown in their present-day positions (panel a) and birth (panel b) positions (in 100 Myr intervals). The red overdensities in panel b primarily reflect the same accreted galaxy observed at different epochs .

2018) by Belokurov et al. (2018), Haywood et al. (2018), and Helmi et al. (2018), giving new weight to the proposed gas-rich merger hypothesis.

As summarised by Helmi (2020), the focus has now shifted from merely identifying accreted stars to characterising the properties of the merging progenitor galaxy and its gas content. Several studies have investigated its global chemical composition (for example Das et al. 2020; Feuillet et al. 2021; Aguado et al. 2021; Matsuno et al. 2021; Buder et al. 2022; Belokurov & Kravtsov 2022; da Silva & Smiljanic 2023; Monty et al. 2024; Ou et al. 2024), while others tried to recover the merger process itself (for example Naidu et al. 2021) as well as the effects of the merger on the existing stars, such as the heating – or *splashing* – of stellar orbits (Di Matteo et al. 2019; Belokurov et al. 2020; Belokurov & Kravtsov 2022). More recently, Skúladóttir et al. (2025), building on N-body simulations by Mori et al. (2024), examined how chemical properties vary with orbital characteristics. Even with fewer than one hundred stars in their updated sample from Nissen & Schuster (2010); Nissen et al. (2024), they successfully separated the accreted stars into more and less bound populations through more or less negative orbit energies and identified statistically significant chemical differences between them. Skúladóttir et al. (2025) interpreted these trends using the scenario proposed by Mori et al. (2024), in which the outer stars of the accreted galaxy—characterised by higher (less negative) orbital energies—were accreted earlier and at larger Galactocentric radii, while stars from the central regions, with lower (more negative) energies, were accreted later and more centrally. The inferred radial gradient in star formation efficiency led to systematically higher [Fe/H] and [Mg/Fe] abundances in stars formed in the former core of the galaxy, a picture consistent with observations of present-day dwarf galaxies (Lucchesi et al. in prep.).

To further test and refine this scenario, we turn to a different simulation suite: the NIHAO-UHD project, which provides high-resolution, fully cosmological zoom-in simulations of Milky Way-type galaxies undergoing satellite accretion (Buck 2020; Buck et al. 2020, 2021). Unlike the idealised N-body simulations by Mori et al. (2024), NIHAO-UHD self-consistently models the chemical and dynamical evolution of stars within a hierarchical cosmological context (Buck et al. 2021). The simulation in particular also includes two post-processing steps that make it particularly well suited to study the chemodynamical memory of the galaxy and its major mergers. Firstly, we have traced the birth positions of stars in discrete 100 Myr time steps, enabling a clean separation of in-situ from accreted stars<sup>1</sup>.

<sup>1</sup> Potential inaccuracies arise around the time of the major merger itself.

Secondly, we have calculated the same integrals of motion, that is orbit energies and actions for the Milky Way analogue simulation that are calculated for stars in our Milky Way galaxy.

Similar analyses of accreted structures in cosmological simulations have been presented by Khoperskov et al. (2023a,b), who examined the phase-space distribution of stellar-halo debris across the HESTIA suite of Local-Group analogues. Their work demonstrated that merger remnants occupy broad and evolving regions in energy-angular momentum and action space and already hinted at correlations between stellar age, chemistry, and binding energy. A complementary study by Khoperskov et al. (2023c) used these simulations to constrain the abundance gradient of the GSE progenitor, establishing a connection between chemical and dynamical memory similar in spirit to the one explored here.

In this first paper (Paper I) we address the following questions:

- (i) What can we learn about the selection efficiency of accreted stars in integrals of motions phase-space (Helmi et al. 2018; Feuillet et al. 2021; Buder et al. 2022; Monty et al. 2024)?
- (ii) What memory of the birth positions and past chemical evolution is retained in integrals of motion space (Skúladóttir et al. 2025)?

Paper II analyses how the effects of the merger process manifest in the simulation, for example through the proposed *splashing* of in-situ star orbits (Belokurov et al. 2020) or mixing of in-situ and accreted gas to form *splashed* stars.

By answering these questions with a Milky Way analogue simulation, we reveal a preserved chemodynamical memory of the last major merger and unveil connections and biases that fundamentally change how we reconstruct the Milky Way’s formative history.

## 2 SIMULATED DATA

In this study we examine the high-resolution cosmological zoom-in simulation g8.26e11, a Milky Way analogue from the *Numerical Investigation of a Hundred Astronomical Objects* (NIHAO) simulation suite (Wang et al. 2015) that includes newly available chemical-evolution tracing (Buck et al. 2021). We use g8.26e11 because, as described below, it closely matches several key Milky Way properties — halo and stellar mass, rotation curve, and a disk-dominated, multi-armed spiral morphology — and it experienced a major merger at a lookback time comparable to the Milky Way’s last major merger. Although the model does not form a strong bar (see Buder et al. 2025), we argue that this is not critical for the questions addressed here.

This galaxy model forms part of the NIHAO-UHD series (Buck et al. 2020) and has been utilised in several prior investigations, including work on the properties of Milky Way satellites (Buck et al. 2019), the spin of the Galactic dark matter halo (Obreja et al. 2022), abundance clustering to reconstruct birth conditions of stars (Ratcliffe et al. 2022), and the redshift evolution as well as shape of radial metallicity gradients in the ISM (Ratcliffe et al. 2025; Buder et al. 2025). A version of this simulation was also employed by Buck et al. (2023) and with reduced mass resolution by Buder et al. (2024) to explore the chemical tagging of stars associated with its last significant accretion event (GSE).

We briefly describe the simulation with reference to the above mentioned works in Sec. 2.1. The main new insights for this simulation are provided by additional information on the birth positions of star particles (see Fig. 1) as well as orbit properties, which we describe in Secs. 2.2 and 2.3, respectively.

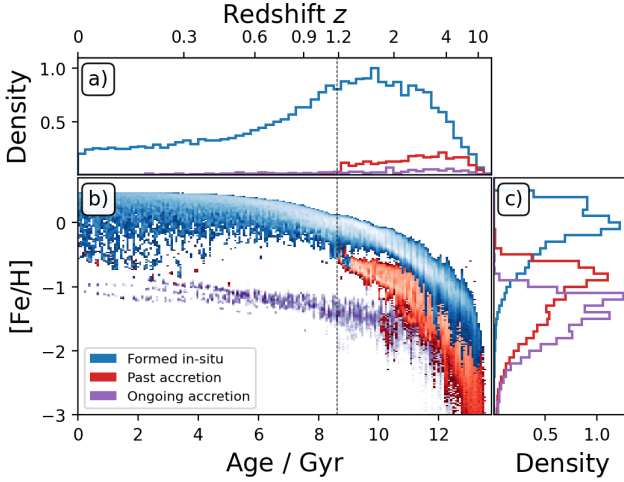


**Figure 2.** Age–metallicity distributions of in-situ (blue), previously accreted (red), and currently accreting (purple) stars, also shown as marginal 2D histograms with age (top) and [Fe/H] (right). A vertical dashed line indicates the time of the major merger around 8.6 Gyr ago (●).

## 2.1 A NIHAO-UHD Milky Way analogue simulation

The simulation was performed using the smoothed particle hydrodynamics code `Gasoline2` (Wadsley et al. 2017), incorporating sub-grid turbulent diffusion, and adopting cosmological parameters from Planck Collaboration et al. (2014). The simulation setup and feedback mechanisms follow the NIHAO framework (Wang et al. 2015), with the zoom-in configuration and baryonic physics described in Buck et al. (2021). Star formation and stellar feedback prescriptions follow Stinson et al. (2006) and Stinson et al. (2013), respectively. Notably, the simulation used here is a more recent, higher-resolution rerun of the model in Buder et al. (2024), and includes updated nucleosynthetic yields.

We focus our analysis on the main halo by identifying it with the Amiga Halo Finder (Knollmann & Knebe 2009), using the build-tin tools of the `PYNBODY` package (Pontzen et al. 2013). To orient the system, we rotate it face-on by aligning the angular momentum vector via `PYNBODY.ANALYSIS.ANGMOM.FACEON`. The simulated disk galaxy with spiral arms has a virial radius of  $R_{200} = 206$  kpc and a total mass (baryons + dark matter) within this radius of  $9.1 \times 10^{11} M_\odot$ . At present-day ( $z = 0$ ), this includes  $8.2 \times 10^{11} M_\odot$  in dark matter,  $6.4 \times 10^{10} M_\odot$  in gas, and  $2.3 \times 10^{10} M_\odot$  in stars. The stellar mass resolution is approximately  $7.5 \times 10^3 M_\odot$  per particle. For this study, we will refer to the galactocentric radius as the three-dimensional spherical radius

$$R_{3D} = \sqrt{x^2 + y^2 + z^2}, \quad (1)$$

rather than the cylindrical one, which is often used when focusing on studies of galactic discs (for example by Buder et al. 2025, for the same simulation).

Due to computational constraints, stars in the simulation are represented by tracer particles corresponding to simple stellar populations of uniform age, metallicity, and initial mass function (IMF). Chemical enrichment is computed using the `CHEMPY` framework (Rybicki et al. 2017), implemented by Buck et al. (2021). We adopt the `alt` configuration, assuming a Chabrier (2003) IMF with a high-mass slope of  $\alpha_{\text{IMF}} = -2.3$ , spanning stellar masses from 0.1 to  $100 M_\odot$ , and covering metallicities  $Z/Z_\odot \in [10^{-5}, 2]$ . The enrich-

ment includes contributions from asymptotic giant branch (AGB) stars, core-collapse supernovae (CCSN;  $8 - 40 M_\odot$ ), and Type Ia supernovae (SNIa), modelled with an exponential delay-time distribution (slope  $-1.12$ ), a minimum delay of 40 Myr, and a normalised rate of  $\log_{10}(N_{\text{Ia}}) = -2.9$  (see Buck et al. 2025; Gunes et al. 2025 for a Bayesian approach to selecting these parameters). Yields are taken from Chieffi & Limongi (2004, CCSN), Seitenzahl et al. (2013, SNIa), and Karakas & Lugaro (2016, AGB; `new_fid` yields in Buck et al. 2021), but no additional contributions, for example from neutron star mergers, for the rapid neutron-capture process. The simulation tracks elemental abundances for H, He, C, N, O, Ne, Mg, Al, Si, P, S, V, Cr, Mn, Fe, Co, and Ba on a Solar abundance scale by Asplund et al. (2009). In alignment with the approach in Buder et al. (2025) and differing from Buder et al. (2024), we adopt the simulated abundances directly, without applying empirical offsets. We note, however, that the median [Fe/H] for stars within a Solar-like galactocentric cylindrical radius of  $R_{\text{GC}} = \sqrt{x^2 + y^2} = 8.2 \pm 0.5$  kpc (Bland-Hawthorn & Gerhard 2016) and Solar-like age of  $4.5 \pm 0.5$  Gyr (Soderblom 2010) is  $+0.15$  dex and thus slightly enhanced with respect to the actual Milky Way. The star formation history, approximated by the stellar age histogram in Fig. 2a, of our analogue and Milky Way estimates (Snaith et al. 2015) is qualitatively similar with a steep rise from high redshifts to cosmic noon (at  $z \sim 2$ ) and a decreasing star formation thereafter. However, both differences in galaxy properties as well as our chosen yields and other chemical evolution parameters can explain the offsets in abundances (see also Buck et al. 2021).

## 2.2 Tracing birth positions for stars of the main galaxy body

In a post-processing step, we have selected all star particles within a radius of 50 kpc from the present-day centre of mass of the simulation box. We then went back to previous simulation snapshots and identified all star particles that were born between timesteps of 100 Myr. We then logged the positions of these star particles relative to the centre of mass of the main halo at the time, effectively tracing the birth positions with respect to the main halo, including birth radii

$$R_{\text{birth,3D}} = \sqrt{x_{\text{birth}}^2 + y_{\text{birth}}^2 + z_{\text{birth}}^2} \quad (2)$$

## 2.3 Orbital properties

The simulation is tracing information on both the Cartesian velocities of each particle  $v_x, v_y, v_z$  as well as the potential  $\phi$  at its current position<sup>2</sup>. This allows us to calculate the specific Newtonian energy  $E$  of the particle (per unit mass) as

$$E = \frac{1}{2} (v_x^2 + v_y^2 + v_z^2) + \phi(x, y, z) \quad (3)$$

In addition to the orbit energy, we also calculate orbit actions  $J_{i \in [R, \varphi, z]}$  as integrals of motion with the `AGAMA` package (Vasiliev 2019). We use `AGAMA.POTENTIAL` to create a multipole expansion of the simulation potential by superimposing the dark matter, star, and gas particles (all weighted by their masses). This composite potential is passed to the `AGAMA.ACTIONFINDER`, which computes the approximate orbital actions ( $J_R, J_\varphi \equiv L_Z$ , and  $J_Z$ ) for any given phase-space point (or in our case star particle) using the fast but approximating Stäckel fudge method (Binney 2012; Sanders & Binney 2015).

<sup>2</sup> This simulation output is `potential_phi` in the simulation FITS file.

### 3 ANALYSIS

The ability to trace stellar birth positions in the NIHAO-UHD Milky Way analogue provides a unique opportunity to evaluate how much chemodynamical information is retained after a major merger. We begin by establishing a broad classification of stars into *in-situ*, past accretion, and ongoing accretion categories (Section 3.1). In Section 3.2, we examine the orbital properties of stars and quantify the efficiency of recovering accreted populations in integrals-of-motion space. Section 3.3 then addresses how well the galaxy preserves its memory of stellar birth positions and chemical evolution in phase-space. Together, these analyses reveal how selection effects shape our ability to reconstruct the progenitor and chemical history of the last major merger.

#### 3.1 Tracing in-situ formation, past accretion, and ongoing accretion

To broadly separate stars by their origin, we adopt a three-part classification: *in-situ formation*, *past accretion*, and *ongoing accretion*. The goal is to construct a simple, interpretable, but still somewhat physically motivated scheme that captures the dominant contributors in each category without invoking overly complex selection criteria. Our classification is thus informed by both the present-day and birth positions of stars in the simulation (Fig. 1) as well as their age-metallicity distribution (Fig. 2). Based on these diagnostics, we define the following three selections.

Stars associated with the infalling dwarf galaxies with lower [Fe/H], selected as part of the sample with

$$\text{Ongoing accretion: } \begin{cases} R_{3D} > 50 \text{ kpc or} \\ E > 0 \text{ kpc km s}^{-1} \text{ or} \\ (\text{age} < 10 \text{ Gyr and } [\text{Fe}/\text{H}] < -1) \end{cases} \quad (4)$$

The last adjustment is included to also identify the full extend of younger stars of the clearly separated dwarf galaxies in Fig. 1b that are already within 50 kpc and already have negative orbit energies.

Stars now within 50 kpc but with signs of external origin at birth are defined as

$$\text{Past accretion: } \begin{cases} R_{3D} \leq 50 \text{ kpc and} \\ E < 0 \text{ kpc km s}^{-1} \text{ and} \\ (R_{\text{birth},3D} > 50 \text{ kpc or } |z_{\text{birth}}| > 5 \text{ kpc}) \end{cases} \quad (5)$$

In particular the selection of stars with  $|z_{\text{birth}}| > 5 \text{ kpc}$  is an important and clean adjustment, as it adds the 28 % of finally selected stars that were born in the last stages of the inclined merger. We have optimised this selection via the position of selected stars in the age-metallicity plane of Fig. 1b.

All remaining stars formed and residing within the central region were defined as

$$\text{In-situ: } \begin{cases} R_{3D} \leq 50 \text{ kpc and} \\ E < 0 \text{ kpc km s}^{-1} \text{ and} \\ R_{\text{birth},3D} \leq 50 \text{ kpc and} \\ |z_{\text{birth}}| \leq 5 \text{ kpc} \end{cases} \quad (6)$$

While our selection is certainly not perfect, it provides a reasonable compromise. Each of the three groups is dominated by stars that plausibly reflect their intended origin, with minimal overlap. 95% of the stars selected as currently being accreted are unbound, that is, have positive specific orbit energies. Similarly, 99% of stars selected as accreted in the past are currently on bound orbits before

enforcing negative specific orbit energies. Tracing the star formation in Figs. 1 and 2, only 6771 star particles (2.7 % of accreted sample) fall into a hard-to-classify category of overlapping chemistry ( $-0.6 < [\text{Fe}/\text{H}] < -0.2$ ) and birth positions between the last stage of the merger around 8.50 and 8.65 Gyr ago. Our selection thus provides a useful basis for subsequent analysis.

Of the  $2.9 \times 10^6$  star particles ( $2.3 \times 10^{10} M_{\odot}$ ), we select 87.9 % ( $2.0 \times 10^{10} M_{\odot}$ ) as *in-situ*, 8.5 % ( $1.9 \times 10^9 M_{\odot}$ ) as previously accreted and 3.5 % ( $8.1 \times 10^8 M_{\odot}$ ) as currently being accreted. At present-day the stellar mass ratio of previously accreted galaxy compared to the Milky Way analogue is 1:11. When only counting stars with ages above 8.6 Gyr ago, that is older than the merger, the mass ratio is 1:5 ( $1.9 \times 10^9 M_{\odot}$  vs.  $9.6 \times 10^9 M_{\odot}$ ).

While versions of Figs. 1a and 2 have already been analysed for a lower resolution version of this simulation by Buder et al. (2024), the pattern of birth positions in Fig. 1b is intriguing, as we can see several overdensities that follow each other like a string of pearls. For each of these pearls, representative of star formation within 100 Myr post-processing steps (see Sec. 2.2), we identify a spatial region within a reasonable age interval (see Tab. A1) that traces the median birth position and then fit and interpolate a smooth function<sup>3</sup> to the discrete positions. We visualise this in Fig. 3 as a golden thread that reliably<sup>4</sup> traces the path of merged galaxy based on the star formation from 12 Gyr ago until its last star formation period during the merger with the analogue around 8.6 Gyr ago. While not the focus of our work, we note that the galaxy that later merged with the Milky Way encountered a merger of its own with another galaxy 10.8 Gyr ago around  $(X_{\text{birth}}, Y_{\text{birth}}, Z_{\text{birth}}) = (-120, 25, -55) \text{ kpc}$  that changed its course. In almost all cases, we see the now accreted galaxy as disk galaxy, most clearly in the almost face-on few of the galaxy across the time steps of Fig. 3c.

We will investigate how birth positions may be related to present-day properties in Sec. 3.3. But first, we provide an overview of orbit properties in the simulated galaxy.

#### 3.2 Dynamic properties and selection efficiency of accreted stars via integrals of motions

As customary in recent observational Galactic dynamical studies (for example Helmi et al. 2018; Trick et al. 2019; Helmi 2020; Buder et al. 2022), we take a look at the distribution of stars in two of the integrals of motion, namely orbit energy  $E$  over angular momentum  $L_Z$  (top rows of Fig. 4) or a condensed version with radial action  $J_R$  over angular momentum  $L_Z$  (bottom rows of Fig. 4 using  $\sqrt{J_R}$ ).

Fig. 4a shows that most of the *in-situ* stars of the spiral galaxy are moving on circular disc orbits as they are concentrated along a curved ridge tracing the maximum angular momentum allowed at each energy. In Fig. 4d, these stars show low radial actions of  $J_R < 10^2 \text{ kpc km s}^{-1}$ . In both figures, we note a broader excess of stars with higher (less negative) orbit energies ( $E > -10^5 \text{ km}^2 \text{ s}^{-2}$ ) and larger radial actions ( $J_R \gtrsim 10^2 \text{ kpc km s}^{-1}$ ) in the area of negligible net rotation ( $L_Z \sim 0 \text{ kpc km s}^{-1}$ ). This region of dynamically hotter stars with more (radially) eccentric orbits is also densely populated

<sup>3</sup> We use SCIPY.INTERPOLATE’s SPLPREP and SPLEV functions (Virtanen et al. 2020) to fit and then evaluate a 2-degree B-spline function with smoothing value 100.

<sup>4</sup> Due to the unstable orientation of the main galaxy for snapshots more than 12 Gyr ago, this reference frame is only reliable to trace the major merger galaxy (visible as several of the grey overdensities in Fig. 3) after the main galaxy’s orientation stabilised.

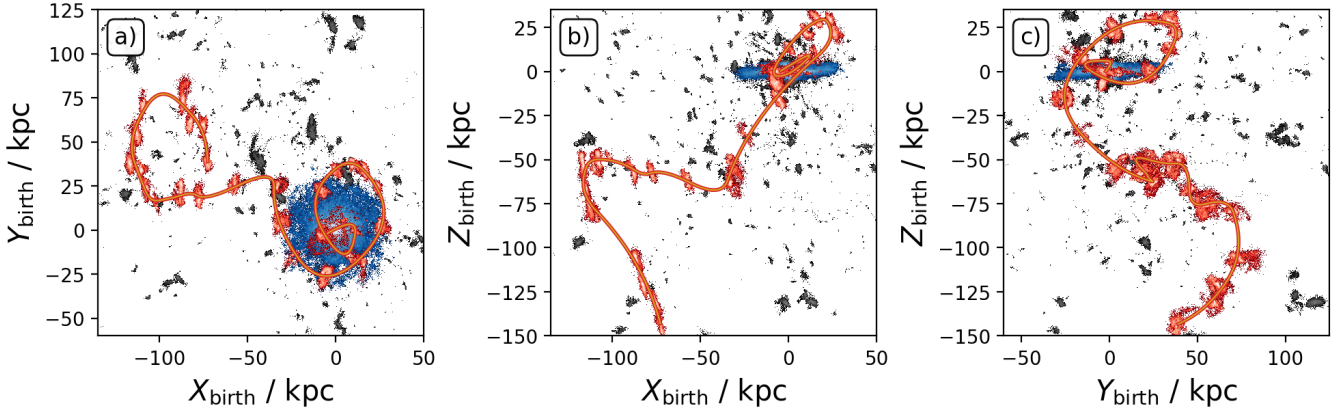


**Figure 3.** Birth positions in different Galactocentric planes of all star particles that are now within 50 kpc (grey density scale), where those born in-situ are in blue and those of the last major merger in red. Birth positions are estimated in 100 Myr steps and thus allow us to follow the changing position of star formation of the now accreted galaxy with respect to the Milky Way analogue. A dark golden line then interpolates the path of the now accreted galaxy

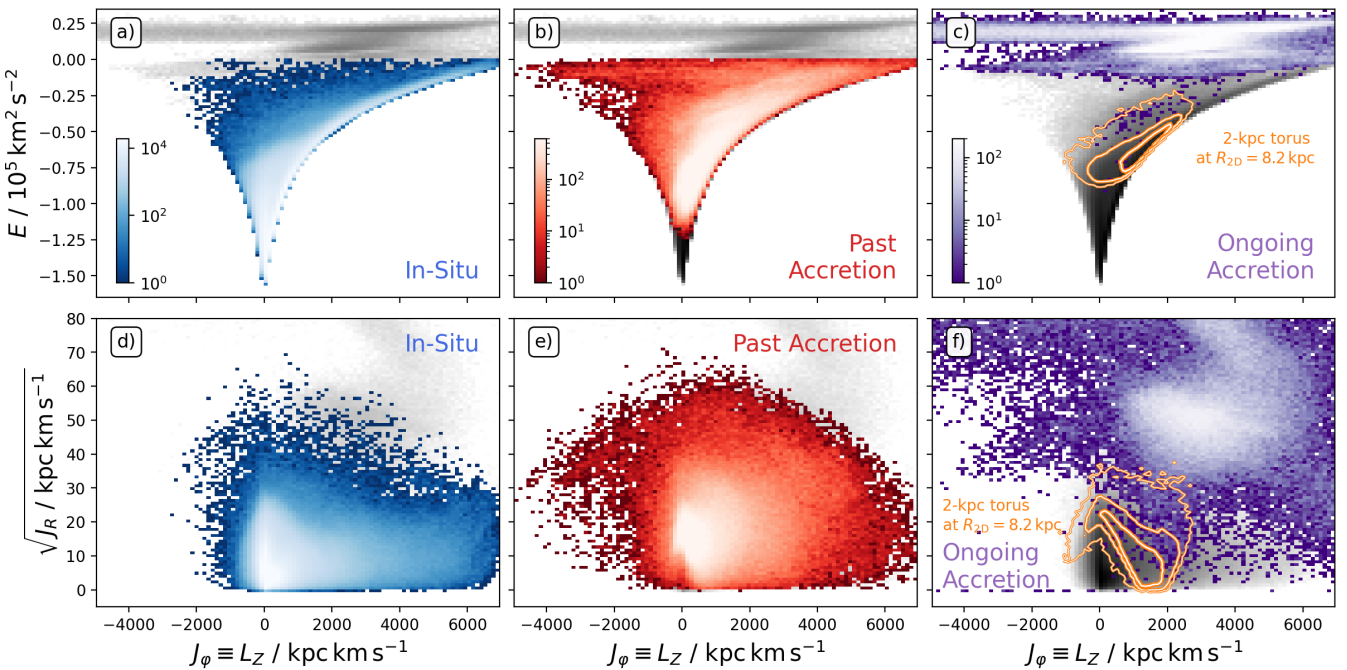


**Figure 4.** Orbit properties of in-situ formed stars (blue, left panels), past accretion (red, middle panels), and ongoing accretion (purple, right panels). Both the specific energy  $E$  (upper panels) and the radial action  $J_R$  (lower panels) are shown with the angular momentum  $J_\varphi \equiv L_Z$ . Stars undergoing accretion, currently located in the Solar-analogue neighbourhood of a 2 kpc torus around  $R_{2D} = 8.2$  kpc, are indicated with orange density contours (the 68th, 95th, and 99.7th percentiles of stars)

by stars that have been accreted previously (see Figs. 4b and 4e around  $L_Z \sim 0$   $\text{kpc km s}^{-1}$ ). The orbits of previously accreted stars extend from these regions of low absolute angular momentum  $|L_Z|$  towards similar positive angular momenta, but show typically higher (less bound) orbit energies and larger radial actions, typical for more radial and eccentric orbits. Stars associated with ongoing accretion (Figs. 4c, 4f), trace partially phase-mixed tidal debris from currently disrupting satellites as well as surviving satellites. They exhibit a wide range in angular momentum, often with retrograde orbits, and occur at high, predominantly positive energies.

As we show the whole galaxy in these figures, we note that the distributions in Fig. 4 look different from what has been found observationally in the Milky Way's Solar neighbourhood (see for example Helmi et al. 2018; Trick et al. 2019; Das et al. 2020; Buder et al. 2022). We have included orange contours in Figs. 4c and 4f which trace the 68th, 95th, and 99.7th percentiles of stars in a torus with a tube radius of 2 kpc at a galactocentric cylindrical distance of  $R_{2D} = 8.2$  kpc, typical of footprints of current Milky Way surveys (for example Abdurro'uf et al. 2022; Katz et al. 2023; Buder et al. 2025). These are distributed mainly within angular momenta

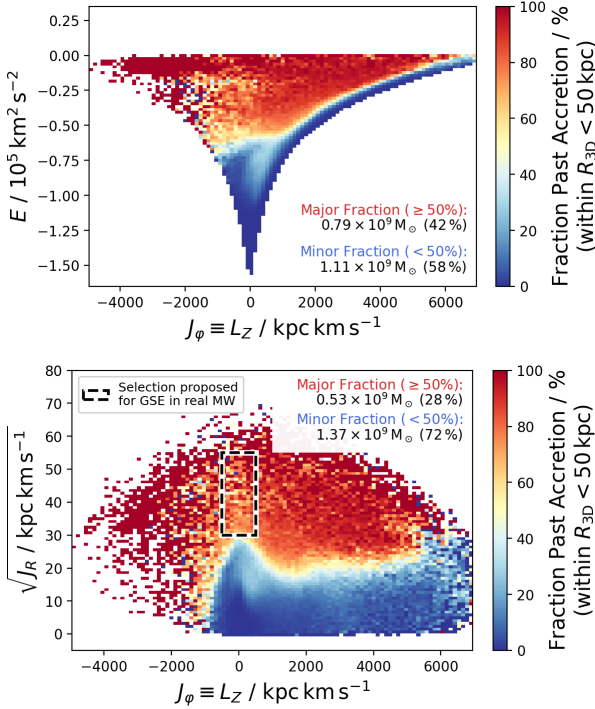


**Figure 5.** Angular momentum  $J_\varphi \equiv L_Z$  vs. Specific energy  $E$  (top panel) and radial action  $J_R$  for stars (bottom panel) for stars within  $R_{3D} < 50$  kpc at redshift  $z = 0$ . Bins are coloured by the fraction of previously accreted stars (defined as Figs. 4b/(a+b) and 4d/(d+e), respectively). We have added the selection proposed by Feuillet et al. (2020) for the real Milky Way as dashed black box. Fig. A1 also includes ongoing accretion in the denominator  $\bullet$ .

of  $0 < L_Z / \text{kpc km s}^{-1} < 2000$  and show circular orbits (low  $J_R$ ) at their largest angular momenta and more eccentric, radial orbits for stars with low absolute angular momenta; in agreement with observations.

In Fig. 4, we are especially intrigued by the extended distribution of accreted stars towards the lowest energies (Fig. 4b) and the significant overlap with the inner in-situ galaxy (Fig. 4a). These are regions that are not extensively explored by surveys of the Solar neighbourhood, but are expected to contain a significant fraction of accreted stars, well hidden within a labyrinth of in-situ stars. We have calculated the relative fraction of previously accreted stars to the main body of the galaxy ( $R_{3D} < 50$  kpc), in Fig. 5. Overall, we see that in-situ stars dominate (blue regions) for specific energies below  $E < -0.58 \times 10^5 \text{ km}^2 \text{s}^{-2}$  as well as radial actions below  $J_R < 20^2 \text{ kpc km s}^{-1}$  and in general stars on circular orbits, with the latter being situated along the right edge of the distribution. Accreted stars dominate (red regions) in the less bound and non-circular regions of the diagrams.

We note the remarkable similarity between Fig. 5 and those presented by Belokurov & Kravtsov (2022, their Fig. 1) and Monty et al. (2024, their Fig. 1) who plot the same plot of angular momentum  $J_\varphi = L_Z$  vs. specific energy  $E$ , but colour-coded by [Al/Fe] and [Eu/Si], respectively. The latter work found a significant change in the median chemical compositions around 50% of the lowest orbit energies for their chosen potentials<sup>5</sup> and attribute them to a transition

<sup>5</sup> The different amplitudes of the orbit energies that mark the boundary between being dominated by accreted or in-situ populations can be explained by both the different actual galaxies and potentials. We find  $-0.66 \times 10^5 \text{ km}^2 \text{s}^{-2}$

of accreted to in-situ stars. We find a similar significant change of the dominant population from accreted to in-situ stars at about 50 % of the lowest orbital energy in our sample. As previously noted, we find that almost half the population of accreted stars is hidden in the region of  $E < -0.58 \times 10^5 \text{ km}^2 \text{s}^{-2}$  that is dominated by in-situ stars. When selecting only from the regions in the  $L_Z$ - $E$  diagram with a fraction of past accretion larger than 50% (orange-red regions in Fig. 5), we only select 42 % of stars of the last major merger.

For the simulated Milky Way analogue, we find that the accreted stars dominate in regions of more radial orbits, typically with  $J_R > 20^2 \text{ kpc km s}^{-1}$  and for the region of  $|L_Z| \lesssim 1000 \text{ kpc km s}^{-1}$  with slightly higher values of  $J_R > 30^2 \text{ kpc km s}^{-1}$ . As we are plotting the whole galaxy in this figure, we include a significant amount of stars with high radial actions, which are typically not visiting the Solar neighbourhood (compare Figs. 4e and 4f and see for example Feuillet et al. 2019). A significant region of the action-action space in the Milky Way is populated by other accreted systems (for example Myeong et al. 2019; Naidu et al. 2020). It is thus not surprising, that the often suggested regions to cleanly select the stars of the last major merger in the Milky Way have been restricted to a small window around  $|L_Z| < 500 \text{ kpc km s}^{-1}$  and  $30^2 < J_R / \text{kpc km s}^{-1} < 55$  (Feuillet et al. 2021; Buder et al. 2022), which we have added to Fig. 5b for reference. Interestingly, our simulation indicates that the suggested lower limit in radial actions coincides with the region where the ratio of accreted to in-situ stars shifts. Contamination thus rapidly increases when accreted stars are selected solely by low radial actions in action space. Buder et al. (2022) found that only  $29 \pm 1$  % of chemically identifiable accreted stars in their sample are within this clean dynamical selection box. Similarly, we find that a restricted selection from Fig. 5 in regions where accreted stars dominate only selects 28 % of all accreted stars (for a study of other selection criteria and their purity as well as completeness see Carrillo et al. 2024).

Comparable overlap between accreted and in-situ stars in  $E$ - $L_Z$  has also been reported in the HESTIA simulations (Khoperskov et al. 2023b), where debris from major mergers spreads across a wide range of energies and angular momenta as the host potential evolves. Their results further showed that the apparent position of merger debris in integral-of-motion space can drift with cosmic time owing to the evolving gravitational potential, consistent with the broad, overlapping distributions seen in our NIHAO-UHD galaxy.

For completeness, we have also calculated the percentage ratio of previously accreted stars to all stars in each of the  $L_Z$ - $E$  and  $L_Z$ - $\sqrt{J_R}$  bins. We append them to this paper in Fig. A1 to visualise the relatively minor contaminating effect of ongoing accretion at higher energies, similar to that of the Sagittarius dwarf spheroidal galaxy in the Milky Way. However, the overall estimate of selecting accreted stars from dominant regions does not shift significantly, that is, only from 42 % to 41 %. Similarly, including ongoing accretion to calculate the fraction in the  $L_Z$  vs.  $\sqrt{J_R}$  domain (compare Figs. 5 and A1) insignificantly changed the selection ratio from 28 % to 26 %. As we are able to use the birth positions for a rather clean selection of in-situ and accreted stars, we can now turn to the analysis of the memory of the progenitor galaxy that might still be imprinted in the present-day properties of the accreted stars.

in our simulation, while Monty et al. (2024) and Belokurov & Kravtsov (2022) find  $-1.6 \times 10^5 \text{ km}^2 \text{s}^{-2}$  and  $-0.75 \times 10^5 \text{ km}^2 \text{s}^{-2}$ , respectively.

**Table 1.** Iron abundances [Fe/H] and stellar masses  $M_\star$  for the four energy-selected zones of previously accreted stars defined in Sec. 3.3. Median [Fe/H] values with 16<sup>th</sup>–84<sup>th</sup> percentiles are shown in Fig. 6. Three logarithmic stellar masses (discussed in Sec. 4.2) are indicated: the total mass of the selected star particles ( $\Sigma$ ), and the inferred masses from the reversed mass–metallicity relations of Naidu et al. (2022a, Eq. 7) and Kirby et al. (2013, Eq. 8).

Energy $E$ $\text{km}^2 \text{s}^{-2}$	[Fe/H] dex	$M_\star(\Sigma)$ $\log_{10} M_\odot$	$M_\star$ (Eq. 7) $\log_{10} M_\odot$	$M_\star$ (Eq. 8) $\log_{10} M_\odot$
$-0.37 \leq$	$-1.4^{+0.5}_{-0.6}$	8.7	7.9	7.9
$[-0.58, -0.37]$	$-1.1^{+0.4}_{-0.6}$	8.7	8.8	8.9
$[-0.77, -0.58]$	$-1.0^{+0.3}_{-0.6}$	8.7	9.1	9.3
$< -0.77$	$-0.9^{+0.3}_{-0.7}$	8.7	9.3	9.5
All energies	$-1.1^{+0.4}_{-0.7}$	9.3	8.8	8.9

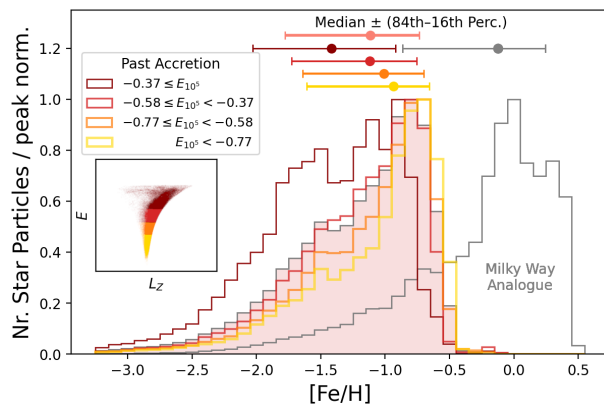


**Figure 6.** Histograms of [Fe/H] distributions of the whole galaxy (grey), and its previously accreted stars with different orbit energies as given in Table 1 (more negative energies from red to yellow, as shown in the inset panel of  $L_z$  vs.  $E$ ). The percentiles of each distribution are plotted at the top right of the figure and show an increase of average [Fe/H] with more negative energies. See [Q](#) for individual figures showing the build-up of this plot.

### 3.3 Dependence of the chemical and birth position on energy

After presenting an overview of the energies and actions of in-situ and, more importantly, accreted stars in the simulation, we focus on how the properties of accreted stars depend on orbital energy  $E$ . This question was already investigated by Skúladóttir et al. (2025), using a small sample of 33 accreted stars with high-quality chemical abundance measurements, which they divide into two samples of 20 and 13 stars with energies above or below  $E = -0.45 \times 10^5 \text{ kpc km s}^{-1}$ , respectively. Our selection of accreted stars consists of a quarter of a million star particles, enabling us to dissect our simulated galaxy into more samples. We thus decide to divide the sample into quartiles, or ‘zones’, of orbit energy, which we list in Table 1 and visualise through the inset shown in Fig. 6.

These four samples, selected to have roughly 25% of accreted stars in each of them, now allow us to investigate the memory or different properties across different orbit energies. In particular, we are interested in the change of the (i) overall metallicity [Fe/H], (ii) chemical abundances, (iii) present-day positions, and (iv) birth positions, which we analyse separately below.

#### 3.3.1 Orbital memory of [Fe/H] abundance

In Fig. 6, we plot the histograms of iron abundance [Fe/H] for the different energy zones with different colours (yellow to dark red for increasing  $E$ ) and the normalised histogram of all accreted stars as filled histogram in the background. The median values of accreted stars ( $[\text{Fe/H}] = -1.1^{+0.4}_{-0.7}$ ) are 1 dex lower than the in-situ galaxy, which has a median  $[\text{Fe/H}] = -0.1^{+0.3}_{-0.5}$ , where the errors are the 16 – 84<sup>th</sup> percentiles. This is consistent with expectations from the mass–metallicity relation (for example Gallazzi et al. 2005; Kirby et al. 2013) and the lower mass of the accreted system in comparison to the main galaxy (1:11).

For most distributions, we see asymmetric, negatively skewed distributions in logarithmic [Fe/H] abundance space, which constitute normal distributions in linear  $N_{\text{Fe}}/N_{\text{H}}$  number density space. Compared to the other zones, the highest orbit energies (dark red) shows a broader and double-peaked distribution. This region is particularly prone to contamination from the many smaller accretion events of metal-poor systems (visible as many smaller dots in Fig. 1b). When comparing our overall selection of accreted stars in this energy zone with those that follow the golden thread of Fig. 3, we find a contamination of up to 50 % for this energy zone. Such a contamination could be limited in the simulation when limiting the selection of the major merger with the birth positions or when using chemical selections in which the different star formation histories of small systems and the major merger galaxy manifest in different enhancement pattern. In observations, these additional aids would, however, either not be available or be observationally expensive. Furthermore, the [Fe/H] distribution of this energy zone, even at its upper end, is lower than those of the other energy zones.

Even when neglecting this zone, we note a decreasing trend of median [Fe/H] from  $-1.1^{+0.4}_{-0.6}$  to  $-0.9^{+0.3}_{-0.7}$  with increasing orbit energy. Both the decrease in [Fe/H] and the non-Gaussian distribution of [Fe/H] for accreted stars with the highest orbit energies agree with the observational findings by Skúladóttir et al. (2025, see their Fig. 3) for the major accretion event in the Milky Way. A similar negative correlation between orbital energy and metallicity is seen in the HESTIA simulations by Khoperskov et al. (2023c, see their Figs. 8 and 9), where the most metal-rich stars of accreted galaxies occupy the lowest energies after merging, while the more metal-poor outskirts populate higher-energy orbits.

#### 3.3.2 Orbit memory of abundances ratios

Having established an energy–metallicity correlation, we are now concerned with the behaviour of elemental abundances beyond [Fe/H]. After having plotted all available abundances<sup>6</sup>, we focus on six of the most insightful abundance combinations in Fig. 7, that is, the abundance planes of  $\log(\text{O/H}) + 12$  vs.  $\log(\text{N/O})$  in Fig. 7a, [Fe/H] vs. [Mg/Fe], [Al/Fe], [Ni/Fe], and [Ba/Fe] in Figs. 7b–e and the observationally found diagnostic plane of accreted stars of [Al/Fe] vs. [Mg/Mn] (Hawkins et al. 2015; Das et al. 2020) in Fig. 7f. In this figure, we trace the running median abundances of the y-axis as dashed lines across 17 equal-number quantile bins<sup>7</sup> in the x-axis. We utilise this method, because neither the median abundance in each dimension, shown as squares in the figure, nor linear functions as used

<sup>6</sup> We attach the remaining elements in Fig. A3, as these either behave similar to the selected elements or might be unreliable due to our limited understanding of their modelling.

<sup>7</sup> To limit the influence of contamination on the trend estimates, we limit the range to the 14<sup>th</sup>..5..99<sup>th</sup> percentiles.

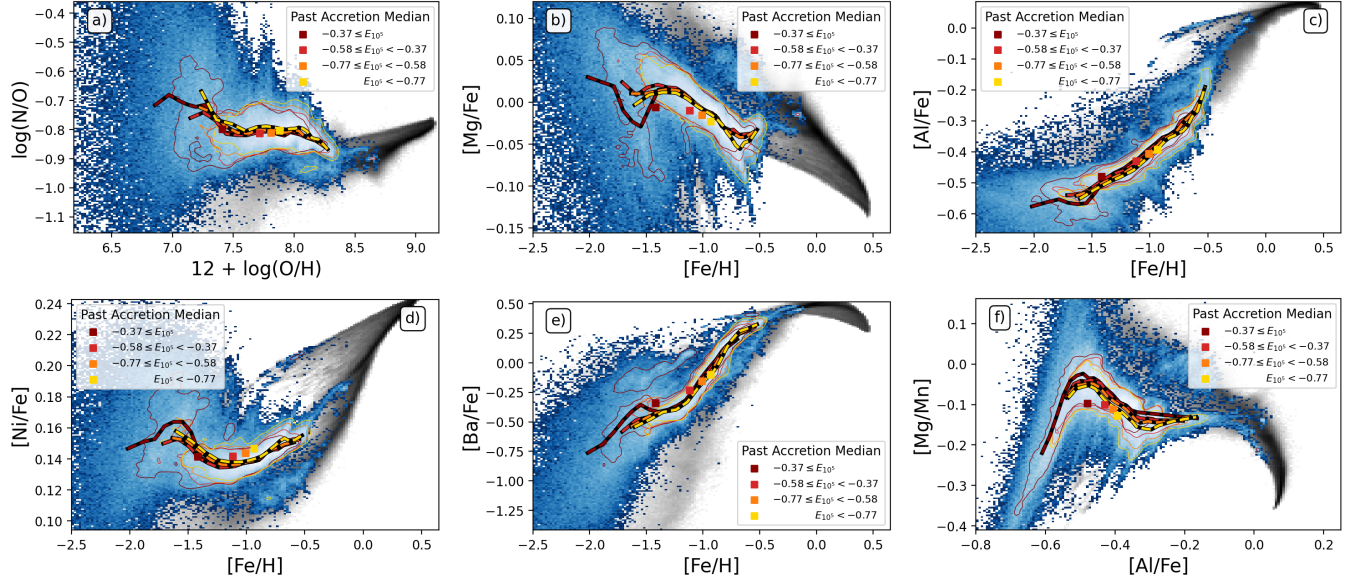


**Figure 7.** Abundance distributions of (past) accreted stars in blue, while the whole simulation is shown in the background (black). Yellow, orange, light and dark red dashed lines show the median abundances for 5-percent-bins if the x-axis of accreted stars for the different energy quantiles (same as in Fig. 6). Narrow contours show the distribution of 68% of each sample. Squares show the median abundances of each sample.

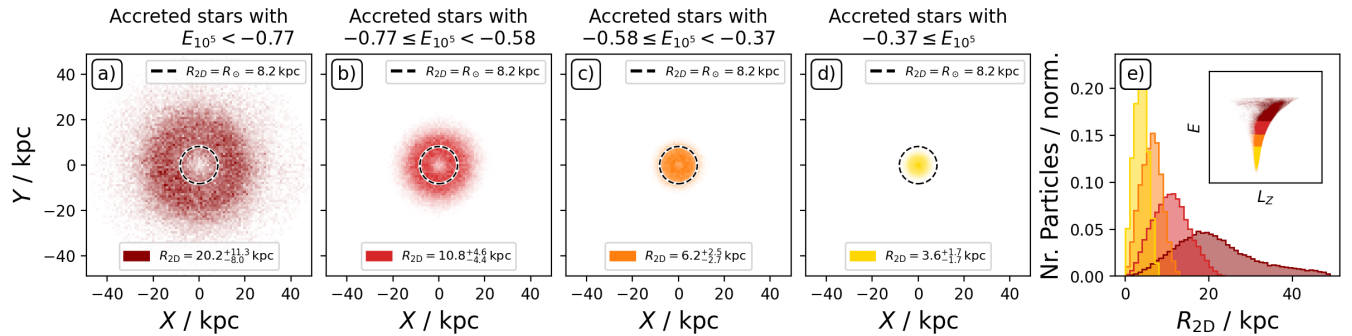


**Figure 8.** Present-day spatial distribution of accreted stars in the Galactocentric  $X$ - $Y$  plane. Panels a-d) show the density distribution of accreted stars with highest to lowest orbit energy quartiles, where the dashed circle shows a solar-analogue  $R_{2D} = 8.2$  kpc. Panel legends list the 50th and 16th-84th percentiles of galactocentric cylindrical radii  $R_{2D}$ . Panel e) shows the  $R_{2D}$  distributions, with an inset visualising the  $L_Z$  vs.  $E$  selection. See Fig. A2 for a similar figure showing the  $X$ - $Z$  plane.

by Skúladóttir et al. (2025), accurately captured the often non-linear abundance distributions. To grasp the extend of abundances covered by each sample, we also show the 68% contours of the different energy samples as narrow lines on top of the density distribution of all accreted stars (blue) and the whole simulation (grey).

For  $\log(\text{N}/\text{O})$  as part of the CNO elements in Fig. 7a, we find that the overall downwards trends of  $[\text{N}/\text{Fe}]$  and  $[\text{O}/\text{Fe}]$  with increasing  $[\text{Fe}/\text{H}]$  lead to rather flat trend of  $\log(\text{N}/\text{O}) \approx -0.8$ . For accreted stars with the highest energies (dark red), we find significantly enhanced ratios of  $\log(\text{N}/\text{O}) > -0.7$  for the lowest oxygen abundances of  $12 + \log(\text{O}/\text{H}) < 7.5$  ( $[\text{Fe}/\text{H}] < -1.5$ ), compared to the other  $E$  zones. These stars, with typical ages of  $11.7^{+1.1}_{-1.4}$  Gyr (or born at redshift  $z = 3.0^{+2.5}_{-1.1}$ ) also exhibit higher abundances of  $[\text{N}/\text{Fe}]$  while showing lower enhancement in the alpha-process abundances (Fig. 7b and Fig. A3 for  $[\text{O}/\text{Fe}]$ ). In combination, they thus have significantly enhanced  $\log(\text{N}/\text{O}) > -0.8$  values, reminiscent of –

but not quite as enhanced as – high-redshift galaxies found by JWST (Cameron et al. 2023; Senchyna et al. 2024; Ji et al. 2025). We notice a small but almost negligible increase  $|\Delta \log(\text{N}/\text{O})| < 0.03$  of median abundances from the stars with the highest (dark red) to those with the lowest energies (yellow). Neither N nor O were analysed by Skúladóttir et al. (2025).

For Mg, one of the  $\alpha$ -process elements,  $[\text{Mg}/\text{Fe}]$  decreases mostly linearly with increasing  $[\text{Fe}/\text{H}]$  among the accreted stars in Fig. 7b, consistent with the onset of SNIa. In addition to low  $[\text{Mg}/\text{Fe}]$  stars in the highest energy group, we also note a slight upturn or spread of  $[\text{Mg}/\text{Fe}]$  of 0.03 dex at the highest  $[\text{Fe}/\text{H}] \sim -0.5$ . Contrary to Skúladóttir et al. (2025), we find very similar median abundance trends without a slope difference (compare to their Fig. 3), consistent with similar abundance trends of accreted systems for  $[\text{Fe}/\text{H}] < -1$  in the HESTIA simulations (Khoperskov et al. 2023c). We do find, however significantly different trends for the highest

$[\text{Fe}/\text{H}] > -0.75$ , where we see both an increase in abundance spread, as well as an upturn of median abundances. This trend is consistent with the findings by Skúladóttir et al. (2025) for their lowest energy sample (compare to their Fig. 5). We notice a similar behaviour of higher abundances for stars with lower orbit energies at similar  $[\text{Fe}/\text{H}]$  for the other  $\alpha$ -process elements, such as Si – again consistent with Skúladóttir et al. (2025) – as well as O, Ne, S, and Ti (Fig. A3). Because the simulation did not include Ca, we cannot compare the trends with those by Skúladóttir et al. (2025), who find less of an increase or spread for this element.

For Al, one of the odd-Z elements, we find a steepening incline  $[\text{Al}/\text{Fe}]$  with rising  $[\text{Fe}/\text{H}]$  of almost 0.3 dex (from  $-0.5$  to  $-0.2$ ), while always staying sub-solar in Fig. 7c. This also constitutes to on average higher  $[\text{Al}/\text{Fe}]$  values for decreasing orbit energies (see median values shown as squares). While the on average higher  $[\text{Al}/\text{Fe}]$  for stars with lower orbit energies agrees with Skúladóttir et al. (2025), they find a flat trend of  $[\text{Al}/\text{Fe}]$  with increasing  $[\text{Fe}/\text{H}]$  (see also Feuillet et al. 2021; Ernandes et al. 2025). However, our trends of a steep increase of abundance agree for Na as another odd-Z element analysed by Skúladóttir et al. (2025, see their Fig. 6), when neglecting the two significant outliers with  $[\text{Na}/\text{Fe}] > 0$ . Albeit not as strong, Belokurov & Kravtsov (2022) also find a slight increase in their accreted populations (see their Fig. 2).

For Ni, one of the iron-peak elements, we find a rather flat trend of  $[\text{Ni}/\text{Fe}]$  with a parabola-like increase of 0.02 dex in either  $[\text{Fe}/\text{H}]$  direction that agrees among the different energy samples. However, due to the different  $[\text{Fe}/\text{H}]$  distributions of the energy samples, this leads to an on average higher  $[\text{Ni}/\text{Fe}]$  with decreasing orbit energy. While Skúladóttir et al. (2025) found an overall slightly decreasing linear trend for  $[\text{Ni}/\text{Fe}]$ , they also find that the  $[\text{Ni}/\text{Fe}]$  is higher for lower orbit energies at the highest  $[\text{Fe}/\text{H}]$ , consistent with the parabola-like shape present in the simulation.

For Ba, one of the neutron-capture elements, we find no clear agreement from the chemical evolution modelling in the simulation to the observational trends of the last major merger in the Milky Way when comparing with the default separation by Skúladóttir et al. (2025, their Fig. 6). We find that Ba, as well as Y and the other neutron-capture elements of the simulation, show a steep and almost linear increase with increasing  $[\text{Fe}/\text{H}]$ , in agreement with predictions by the HESTIA simulations for accreted systems (Khoperskov et al. 2023c). Skúladóttir et al. (2025) find a decreasing trends for  $[\text{Y}/\text{Fe}]$  in the observational data and an even more complicated scattered picture for  $[\text{Ba}/\text{Fe}]$ . We note though, that these disagreements can be reconciled for  $[\text{Ba}/\text{Fe}]$ , when treating the three most metal-poor stars on low orbit energies as outliers in Fig. 6 of Skúladóttir et al. (2025). In that case, their trend of  $[\text{Ba}/\text{Fe}]$  could be interpreted as a steep and linearly inclining trend with increasing  $[\text{Fe}/\text{H}]$  and decreasing orbit energy – now consistent with the simulation predictions. This is remarkable, as the nucleosynthesis tracing of neutron-capture elements is incomplete in the simulation due to the missing prescriptions for enhancement channels beyond CC-SN, SNIa, and the contribution from AGB stars.

For the often used diagnostic plot of accreted stars,  $[\text{Al}/\text{Fe}]$  vs.  $[\text{Mg}/\text{Mn}]$ , we find a trend of decreasing  $[\text{Mg}/\text{Mn}]$  and increasing  $[\text{Al}/\text{Fe}]$  for the decreasing orbit energies. In the simulation, these trends are driven by the difference in Al and Mg, respectively, since Mn is showing a less pronounced change. We note though, that the combination of  $[\text{Mg}/\text{Mn}]$  leads to a slightly more pronounced energy-dependent spread of median abundances of up to  $|\Delta[\text{Mg}/\text{Mn}]| = 0.05$  between the highest and lowest energy zones across the  $[\text{Al}/\text{Fe}]$  range.

Across all figures we find that the median abundance trends be-

tween different energy levels are rather similar and less pronounced than the observational trends found by Skúladóttir et al. (2025). Secondly, we find that the abundances tend to not exactly follow a linear trend, as fitted by Skúladóttir et al. (2025), but a more complex, non-linear behaviour in agreement with predictions by Khoperskov et al. (2023c).. In combination with the different  $[\text{Fe}/\text{H}]$  distributions of the different energy samples, this leads to noticeable differences in the median abundances. Especially when comparing with the abundances trends for the lower energy cuts by Skúladóttir et al. (2025, their Fig. 5), we find very good agreement in the relative abundance changes between their lower and higher energy samples, in particular for the highest  $[\text{Fe}/\text{H}]$  regime.

As the simulation necessarily relies on specific choices for nucleosynthesis channels and stellar yields, we note that both the absolute abundance differences between accreted and in-situ populations and the intrinsic abundance spreads within each population are significantly smaller than observed in the Milky Way. This highlights a general caveat of our analysis: while the relative trends are informative, the absolute abundance scales and dispersions should not be over-interpreted, as they are sensitive to the adopted yields and chemical-evolution prescriptions (see Buck et al. 2025; Gunes et al. 2025, for machine learning methods and model comparison approaches to select chemical enrichment models).

### 3.3.3 Orbit memory of present-day positions

Having found that the orbit energy is correlated with metallicity and elemental abundances, we are now interested in understanding where the accreted stars with different orbit energies are distributed within the Milky Way analogue. In Figs. 8, we therefore show the distribution of the accreted stars from the four energy zones in the  $X$  vs.  $Y$  projection<sup>8</sup>. Since the lower orbit energies correlate with lower radial actions, we of course find that the stars with lower energies are more restricted to the inner galaxy. We find 68 % of the stars with  $E > -0.37 \times 10^5 \text{ kpc km s}^{-1}$  currently have Galactocentric cylindrical radii and heights of  $R_{2D}$  of  $20.2^{+11.3}_{-8.0} \text{ kpc}$  and  $z$  of  $0.2^{+8.9}_{-8.5} \text{ kpc}$ , respectively, whereas the stars with  $E < -0.77 \times 10^5 \text{ kpc km s}^{-1}$  have radii  $R_{2D}$  of  $3.6^{+1.7}_{-1.7} \text{ kpc}$  and  $z$  of  $0.0^{+1.3}_{-1.3} \text{ kpc}$ , respectively. This means that more metal-rich accreted stars are expected to be found closer to the Galactic centre. We will discuss the implications of this finding for strategies needed to find informative surviving members of the last major merger of the Milky Way in Section 4.2.

### 3.3.4 Orbit memory of birth positions

A major motivation of our study is to investigate if there is any memory of the birth positions of accreted stars left in their orbits. Skúladóttir et al. (2025) approached this question forward-looking, by tagging the radius of particles within the smaller galaxy in the simulation by Mori et al. (2024) before the merger and then tracing the time of pericenter passages and present-day orbit properties. In a variation of this approach, our post-processing of birth positions allows us to simply use the birth positions and colour them by their present-day orbit energies. By focussing on two specific regions of birth positions in the  $X_{\text{birth}}$  vs.  $Y_{\text{birth}}$  direction in Fig. 9, we are effectively tracing the star formation (with a resolution of  $\sim 100 \text{ Myr}$ ) of the galaxy long before the merger (Fig. 9a, showing star formation between 11.65 and 10.25 Gyr ago), as well as before and during the

<sup>8</sup> We completeness, we also attach the  $X - Z$  projection in Fig. A2.

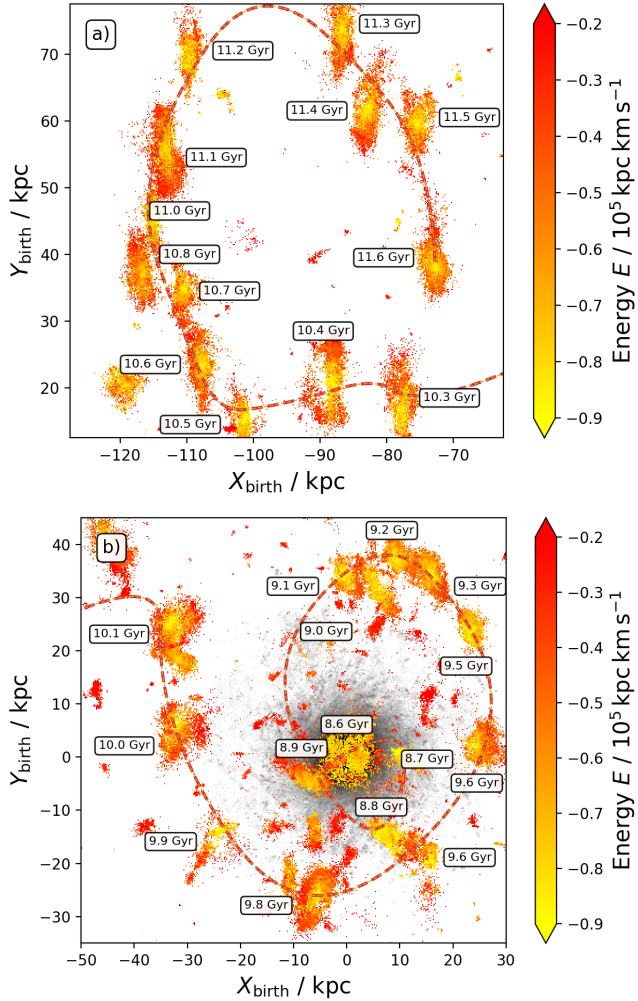


**Figure 9.** Birth positions (determined in batches of 100 Myr) coloured by present-day orbit energy, both before the major merger (top, for star formation between 11.65 and 10.25 Gyr ago) and just before and during the merger (bottom, for star formation between 10.15 and 8.55 Gyr ago), with the main galaxy’s birth positions visible in greyscale. 

merger (Fig. 9b, showing star formation between 10.15 and 8.55 Gyr ago) with the main galaxy (grey background).

A striking feature of basically all de-facto snapshots of star formation is that the stars born in the outskirts of the progenitor now have high orbit energies (are coloured red), while the stars in the centre of the progenitor in each 100 Myr snapshot have low orbit energies (yellow). This is fully consistent with the conclusions drawn by Skúladóttir et al. (2025) as well as Khoperskov et al. (2023b) that stars born in the outskirts of the accreted galaxy have higher orbit energies and stars born in its core have lower orbit energies.

## 4 DISCUSSION

In this paper (Paper I), we have posed three key questions regarding the information recoverable from integrals-of-motion space. We now address these in turn. In Section 4.1, we discuss the efficiency and biases in selecting accreted stars. In Section 4.2, we consider the implications of these findings for future observational strategies to

identify informative members of the Milky Way’s last major merger, GSE. In Section 4.3, we discuss what chemical and birth position memory of the progenitor galaxy is retained in integrals-of-motion space. Together, these results highlight both the opportunities and the limitations in reconstructing the Milky Way’s merger history from present-day phase-space substructures (see also Thomas et al. 2025).

### 4.1 Selection effects of accreted stars in integrals of motion space

Our investigations in Section 3.2 showed that the true extent of accreted stars in the simulated Milky Way analogue extends far into the inner galaxy, which is dominated by in-situ stars. This dominance explains why current observational research on the extent of accreted stars has identified a rather sharp transition at specific orbit energies or radial actions between in-situ and accreted stars of the GSE (Helmi et al. 2018; Feuillet et al. 2021; Monty et al. 2024).

However, our results show that significantly more accreted stars are present with energies and radial actions below the observationally suggested limits in  $E$  (Helmi et al. 2018; Monty et al. 2024) and  $J_R$  (Feuillet et al. 2020, 2021). Importantly, we find 42 % and 28 % of the accreted stars in regions that are dominated by in-situ stars on these low-energy orbits. The dynamical overlap of in-situ and accreted structures is significant and spectroscopic, that is, chemical insights are needed to separate in-situ from accreted stars (for example Das et al. 2020; Horta et al. 2021; Sestito et al. 2021; Buder et al. 2022). A comparable behaviour has been found in the HESTIA cosmological simulations by Khoperskov et al. (2023b), who showed that accreted stars penetrate deeply into the inner few kiloparsecs and overlap strongly with in-situ populations in  $E$ – $L_z$  space.

While several accreted stars and even structures have been found in the inner Galaxy thanks to infrared spectroscopy (for example Horta et al. 2021), this region remains mostly out-of-reach for high-precision optical spectroscopy and partially even astrometry (Queiroz et al. 2023).

The current dedicated spectroscopic searches for accreted stars, which are typically limited to either the nearby or extended Solar neighbourhood (for example Nissen & Schuster 2010; Buder et al. 2022) or far away from the Galactic disc (Naidu et al. 2020) can provide significant insights, but are expected to be not only incomplete but also significantly biased because of the subsample of GSE stars that they are able to target. We remind ourselves that in the simulation, the spatial distribution of the lowest-energy accreted stars is limited to within  $R_{2D} = 3.6^{+1.7}_{-1.7}$  kpc and  $Z = 0.0^{+1.3}_{-1.3}$  kpc (see Figs. 8 and A2). Assuming the distribution of accreted stars would be the same for the Milky Way, we would thus not expect a lot (or any) of the accreted stars with lowest energies to be present in the sample of 33 accreted stars in the Solar neighbourhood by Nissen & Schuster (2010), but mainly those with  $E > -0.57 \times 10^5$  kpc km s $^{-1}$ , consistent with the sample studied by Skúladóttir et al. (2025). The same holds true for Milky Way halo studies (Naidu et al. 2020), which have helped us to better understand the substructure of accretion, but are expected to mostly target GSE stars with  $E > -0.77 \times 10^5$  kpc km s $^{-1}$ . More generally, we expect different [Fe/H] distributions to be recorded depending on the heights and radii of targeted accreted stars, as shown for a selection of radii in Fig. 10. This could potentially contribute to the differences of the [Fe/H] distribution of the observed GSE by Das et al. (2020), Naidu et al. (2020), Feuillet et al. (2020, 2021), and Buder et al. (2022) who analysed the different observations of the APOGEE, H3, SkyMapper, Gaia, and GALAH surveys (for a comparison of their reported [Fe/H] distributions see Fig. 10 by Buder et al. 2022).

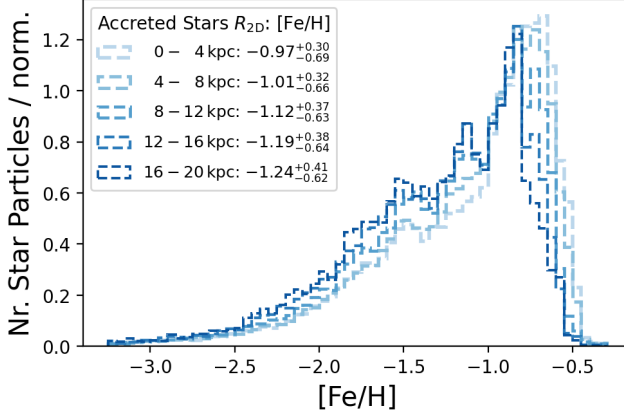


**Figure 10.** Histograms of [Fe/H] distribution for accreted stars with different present-day galactocentric radii  $R_{2D}$  with median [Fe/H] indicated in the legend for each region

Our simulation data suggests that we will find a currently under-represented subset of stars in the inner Galaxy, more specifically within its bulge region. Over the decades (see for example [Barbuy et al. 2018](#), for a review), this dense region has been the target of several dedicated spectroscopic studies (for example [Ness et al. 2013a; Bensby et al. 2017; Lucey et al. 2019](#)). This raises the question if some accreted stars have already been observed by chance. [Ness et al. \(2013a,b\)](#), for example, have identified specific overdensities in the metallicity distribution functions of the bulge region (i.e., below the center at  $b = -5$  deg), namely at  $[\text{Fe}/\text{H}] \in [-1.73, -1.16, -0.66, -0.26, +0.12]$  with typical spreads of  $\pm 0.11 - 0.15$  (see also [Portail et al. 2017](#)). Despite some differences between the actual peak positions (compare for example Fig. 4 by [Barbuy et al. 2018](#)), different studies agreed with the presence of multiple overdensities. [Bensby et al. \(2017\)](#) found the second-lowest metallicity peak around  $[\text{Fe}/\text{H}] = -1.09$ . [Portail et al. \(2017\)](#) also found a peak at  $-1.18 \pm 0.14$  with less (to no) net rotation, reminiscent of the characteristic [Fe/H] and  $L_Z$  distribution of accreted stars.

When focusing on the inner region of the Milky Way analogue ( $R_{2D} < 3.6$  kpc and  $|Z| < 1.3$  kpc), we also find a multi-modal metallicity distribution (see Fig. 11a). The distribution is overall shifted to higher [Fe/H] values than the Milky Way by  $\sim +0.3$  dex compared to the measurements in the Milky Way bulge (see above). Taking this into account, we would expect the accreted stars to contribute mainly to the peak around  $\sim -0.8$ . We can confirm this when selecting the accreted stars of the simulation (golden in Fig. 11a and zoomed in vertically for better visibility in Fig. 11b). What strikes us here is the limited contribution of accreted stars to the inner galaxy (only 2%) but especially to the peak itself. This suggests two things: firstly that the amount of accreted stars distributed in the inner galaxy is insignificant (on a relative level) and secondly that there are still stars formed with the same, outstanding iron abundance as the accreted stars. A simple explanation could be that these particular stars formed from gas of the accreted galaxy – an exciting avenue for quantifying the amount of metal-poor gas brought in by the accreted galaxy ([Buck et al. 2023](#)). This hypothesis should be followed up in a future study that dives into the detailed tracing of the gas of the simulation during the merger. In any case, we do note that the number of stars born with this iron abundance – and in particular those contributing to the bump around  $[\text{Fe}/\text{H}] \sim -0.75$  in the simulation – appears insignifi-

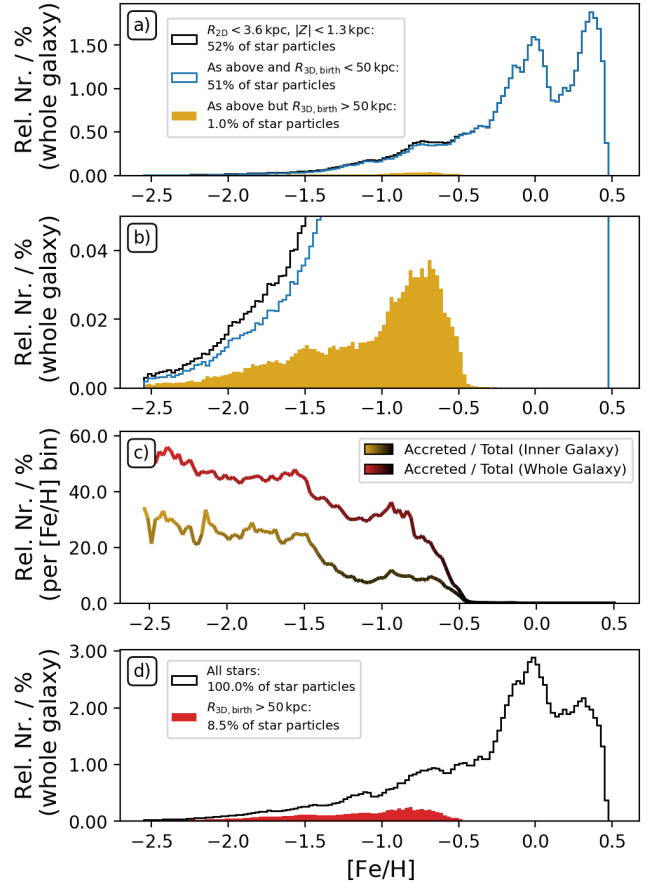


**Figure 11.** Metallicity distribution functions (relative to total number of stars in the galaxy). Top panel shows the distribution of the inner  $R_{3D} < 3.6$  kpc and how in-situ (blue) and accreted populations (golden) contribute to it. Panel b) is showing the same golden distribution of accreted stars as panel a), but zooming vertically in to see more details. Panel c) traces the relative fraction of accreted stars to all stars in the inner galaxy (yellow-black line) as well as the galaxy overall (red-black line). Panel d) shows the distribution of the whole galaxy (black) and all accreted stars (red)

cant compared to the rest of stars in this inner region. A blind survey of 100 stars in this region would be expected to only find 2 accreted stars on average, whereas a survey that is able to preselect stars of the inner galaxy with  $[\text{Fe}/\text{H}] < -0.5$  would be able to increase the sampling rate by at least a factor of 5 to 10 – 30 % (Fig. 11c). Although the overall contribution of accreted stars to the present-day stellar distribution is around 9% (see Fig. 11d), blindly sampling accreted stars is more successful in regions with less metal-rich stars, such as the Galactic halo, as already well established by observations of the Milky Way (e.g. [Conroy et al. 2019](#)).

The question therefore arises, if we perhaps have not actually **observed a significant fraction of** the core of the GSE progenitor yet, since **it is** so well hidden in the centre of our Galaxy. While focussing on a larger metallicity-range in the metal-poor inner bulge, we note that [Lucey et al. \(2022\)](#) only found a small number and percentage of stars with accretion-like, sub-solar  $[\text{Al}/\text{Fe}]$  and  $[\text{Mn}/\text{Fe}]$  in their sample (see their Figs. 7 and 8). Such stars certainly should be followed up to identify if they are part of the accreted population of the GSE (see also [Kunder et al. 2025](#)).

An observation that has previously been debated as a potential

finding of the core of the last major merger of the Milky Way was the Heracles substructure (Horta et al. 2021), with some of the lowest energies of accreted stars found so far. While some researchers have argued that its seemingly distinct separation from the *GSE* in the  $L_Z$  vs.  $E$  could have been caused by bar interactions (Dillamore & Sanders 2025), our findings from the simulation suggest that its metallicity (relative to the *GSE*) is in fact too low to be part of the same system. We thus agree with Horta et al. (2021) that this system is likely a separate accretion event within the Milky Way.

Looking into the near future, the 4MOST survey’s 4MIDABLE consortium surveys of the inner galaxy (Bensby et al. 2019; Chiappini et al. 2019) will observe millions of stars towards this region. If the last major merger in our Milky Way is comparable to the one in our analogue simulation, we expect these surveys to observe a considerable number of accreted stars. More generally looking at observations of the inner galaxy, if one could preselect stars with  $[\text{Fe}/\text{H}] < -0.5$  for spectroscopic follow-up to measure Na or Al as well as Mg and Mn, our simulation data suggests an increase of the ratio of accreted stars in the inner Galaxy from 2 % with a blind selection to 10 % with a metallicity-cut. Preselection methods based on photometric data (e.g. Pristine, SkyMapper; Starkenburg et al. 2017; Da Costa et al. 2019) or on spectrophotometric combinations of *Gaia* BP/RP spectra and Pristine photometry (Martin et al. 2024) have already proven effective in the inner Galaxy (e.g. with the Pristine Inner Galaxy Survey; Arentsen et al. 2020a,b). Comparable strategies could be applied to future infrared surveys such as APOGEE/SDSS (Santana et al. 2021). Subsequently we discuss why such observations could be key for our understanding of the last major merger of the Milky Way by allowing us to better quantify the amount of low-energy *GSE* members.

#### 4.2 The importance of finding low-energy *GSE* members

What could be the potential impact of missing out on the hidden low-energy members of the *GSE*? The detailed impact of the major merger will lie in the impact of the accreted gas and stars onto the chemical make-up and rotation of the Galaxy as well as the merger configuration and pathway. Two general galaxy properties – galaxy mass or mean metallicity – are often used to quantify a galaxy and its potential impact during a merger. With the observationally found mass–metallicity relation (for example Gallazzi et al. 2005; Kirby et al. 2013), these numbers are correlated and allow to roughly estimate the mass of a system from its metallicity and vice versa. In the Milky Way, this relation has been confirmed with surviving smaller galaxies (Kirby et al. 2013) and then used to estimate the masses of disrupted galaxies by comparison (for example Helmi et al. 2018) – in addition to dynamical mass estimates from simulations that recovered the dynamical signatures of the disrupted galaxies (for example Naidu et al. 2022a).

By comparing the mass–metallicity relations of observed surviving and (partially or fully) disrupted dwarf galaxies, Naidu et al. (2022a) uncovered a significant offset between them, with the latter’s metallicities being on average 0.30 dex lower. This difference challenges the assumption of a universal mass–metallicity relation. However, if the preselection methods discussed above preferentially include or exclude stars of certain metallicities, part of the observed offset could arise from selection effects, in addition to potential differences stemming from continued chemical enrichment in surviving systems compared to quenched evolution in disrupted ones, as seen for example in the HESTIA simulations by Khoperskov et al. (2023c). Beyond the biases for *GSE* (Skúladóttir et al. 2025), we are wondering if the  $[\text{Fe}/\text{H}]$  estimates of surviving dwarf galaxies could be biased by the

analysis of stars in their cores (and less so their outskirts), whereas the  $[\text{Fe}/\text{H}]$  estimates of disrupted dwarf galaxies could be biased towards lower values by the stars in their previous outskirts, rather than their more metal-rich cores (which our simulations suggest to be more likely embedded in the inner galaxy regions dominated by in-situ stars). To visualise this point, we are recreating the mass–metallicity relation as shown by Naidu et al. (2022a) in Fig. 12. To this figure, we add the median  $[\text{Fe}/\text{H}]$  values for the four different energy zones of the accreted stars in our simulation (with yellow to dark red corresponding to the lowest to highest energy zones from Fig. 6). We indeed see that when selecting preferentially (or even only) the higher energy samples, we tend to infer a lower  $[\text{Fe}/\text{H}]$ . The lower-energy samples would increase the average median  $[\text{Fe}/\text{H}]$ . We also notice that shape – in particular the non-Gaussianity – of the metallicity distribution functions of a galaxy needs to be included into this figure for both surviving and disrupted dwarf galaxies, rather than the currently used mean or median  $[\text{Fe}/\text{H}]$ .

To estimate the potential impact of systematic offsets of metallicities, we invert the published stellar mass–metallicity relations for dwarf galaxies. Following Naidu et al. (2022a), we adopt either their relation for disrupted dwarfs (their Eq. 3),

$$\log_{10}(M_\star/\text{M}_\odot) = 2.78 \times [\text{Fe}/\text{H}] + 11.86, \quad (7)$$

or the relation for surviving dwarfs from Kirby et al. (2013), shifted by  $-0.30$  dex,

$$\log_{10}(M_\star/\text{M}_\odot) = 3.33 \times [\text{Fe}/\text{H}] + 12.63. \quad (8)$$

Inserting the median  $[\text{Fe}/\text{H}]$  values of the four orbital-energy zones, we infer the logarithmic stellar masses of  $\log_{10}(M_\star/\text{M}_\odot) \approx 7.9\text{--}9.5$  listed in Tab. 1. This range spans  $\sim 1.6$  dex, that is, a factor of  $\sim 40$  in stellar mass, depending on which part of the progenitor is sampled.

This exercise illustrates that chemically inferred stellar masses are highly sensitive to the adopted metallicity distribution and to the choice of mass–metallicity relation. In a future project, we will therefore re-assess the mass–metallicity relation in detail, accounting for full metallicity distributions and for potential systematic differences between disrupted and surviving dwarf galaxies.

#### 4.3 Chemical and birth position memory of the progenitor galaxy in integrals of motion space

Throughout our analysis in Section 3.3, we have investigated if we can find the same patterns from the observational study by Skúladóttir et al. (2025) that accreted stars with different orbit energies carry both chemical and birth position memory.

Indeed, we have found correlations of present-day orbit energy and metallicity (Fig. 6) as well as chemical enhancement of several individual elements (Fig. 7), but also a correlation with present-day orbits (Figs. 8 and A2) and most importantly birth positions (Fig. 9). While these findings are all in agreement with the findings by Skúladóttir et al. (2025) at face value, here we want to discuss a few more subtle differences that we note because of our larger sample size that also reaches towards the lower-energy regions and thus the core of the major merger galaxy.

Because of the low number of only 33 targets, Skúladóttir et al. (2025) could only subdivide their sample into two groups. To quantify the abundance differences between the groups beyond computing abundance offsets, they fitted linear functions in  $[\text{Fe}/\text{H}]$  vs.  $[\text{X}/\text{Fe}]$  space and were able to identify both overall offsets and linear, that is, metallicity-dependent trends. However, the abundance trends of our simulation in Fig. 7 often show non-linear trends, which would be

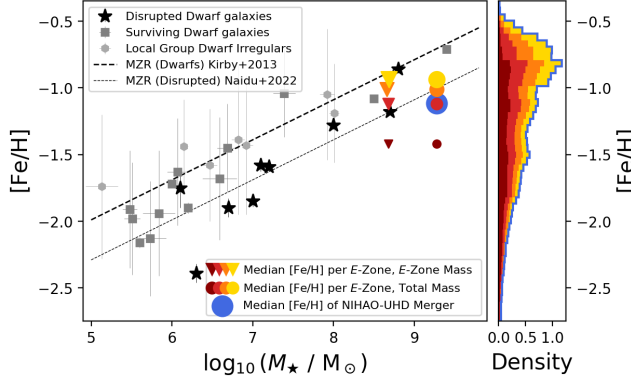


**Figure 12.** Mass-metallicity relations (dashed lines) for different galaxies and selections. We list both reported measurements of disrupted (black star symbols), surviving (grey squares), and irregular dwarf galaxies (grey circles) by Kirby et al. (2013) and Naidu et al. (2022a). For the major merger of the NIHAO-UHD Milky Way analogue we show both the median [Fe/H] and total mass for the whole merger (blue dot), and median [Fe/H] of the different energy zones vs. the total merger mass (coloured dots); and only the masses of star particles in the individual energy zones (coloured triangles). Right panel shows the stacked histograms of the different metallicity distributions following the same colour code

insufficiently covered by linear functions. In particular, we note a shift of the skewed metallicity distribution function with decreasing orbit energy from metal-poor to metal-rich. Skúladóttir et al. (2025) have in fact made a similar discovery in their research, when assessing the impact of the energy cut onto the metallicity distribution function (see their Appendix A), where moving their energy cut to lower energies limits the sample to quite high  $[\text{Fe}/\text{H}] \gtrsim -0.9$  and reveals two significantly different distributions, in line with our findings. Again in line with our findings, they found significantly different abundance patterns, especially for  $[\text{Fe}/\text{H}] > -1$ .

Because of the changing metallicity distribution function and some non-linear trends in  $[\text{X}/\text{Fe}]$  in our larger – but simulated – sample, we believe that future investigation of observed abundance trends – in the best case with larger samples across a diverse energy range – should aim to go beyond the fitting of linear trends to these distributions as done by Skúladóttir et al. (2025).

Our investigations confirm the conclusions drawn by Skúladóttir et al. (2025), that the lower-energy stars were born in the inner parts of the now-accreted galaxy, whereas higher-energy stars were born in its outskirts. Similarly, the combination of our investigation and the findings by Skúladóttir et al. (2025) suggests that the GSE was a disk galaxy with a noticeable radial metallicity gradient, consistent with the HESTIA results by Khoperskov et al. (2023c), who found that accreted disk-like satellites typically display pronounced internal  $[\text{Fe}/\text{H}]$  gradients of  $\sim -0.10 \text{ dex kpc}^{-1}$ , preserving their chemical stratification even after full disruption. Similar to the findings by Carrillo et al. (2025) with Auriga simulations, our investigation of a cosmological zoom-in simulation thus supports and extends these findings, reinforcing that the GSE progenitor had a clear radial metallicity gradient. This provides rare direct evidence of internal chemical structure in an accreted galaxy and is yet another confirmation that GSE likely experienced extended, inside-out star formation before merging with the Milky Way.

## 5 CONCLUSIONS

We have used a high-resolution NIHAO-UHD cosmological simulation to study the last major merger of a Milky Way analogue, addressing three key questions:

First, the present-day orbital properties of accreted stars correlate with their birth radii within the progenitor galaxy (Sec. 4.1), consistent with similar findings from the HESTIA simulations (Khoperskov et al. 2023b).

Second, these correlations arise from abundance gradients within the progenitor, in line with the internal metallicity gradients found in accreted progenitors in other simulations Khoperskov et al. (2023c,a); Carrillo et al. (2025). Lower-energy stars, now more strongly bound to the Milky Way, formed in the core of the accreted galaxy and are systematically more metal-rich and chemically enhanced. This supports the scenario of Skúladóttir et al. (2025) and demonstrates that chemodynamical memory is preserved across the merger. However, accreted stars also extend to much lower orbital energies and radial actions than previously inferred. As a consequence, selection methods in integrals-of-motion space (Helmi et al. 2018; Feuillet et al. 2021; Monty et al. 2024) systematically miss stars from the progenitor’s core. Progenitor reconstructions are therefore biased toward the chemically metal-poor outskirts. These biases may even help explain differences in the mass–metallicity relation between surviving and disrupted dwarf galaxies (Naidu et al. 2022b), offering a testable prediction for future work (Sects. 4.3 and 4.2).

Third, our analysis shows that current selection functions alone are insufficient to capture the full abundance distribution of the progenitor. Future survey strategies must target inner-Galaxy stars to recover the missing, chemically enriched core population.

Finally, our findings highlight the power of cosmological simulations to quantify biases introduced by observational selection functions, and to guide strategies for building a more representative census of accreted stars in the Milky Way.

## ACKNOWLEDGMENTS

We acknowledge the traditional owners of the land on which the ANU stands, the Ngunnawal and Ngambri people. We pay our respects to elders past, and present and are proud to continue their tradition of surveying the night sky and its mysteries to better understand our Universe. SB acknowledges support from the Australian Research Council under grant number DE240100150. TB’s contribution to this project was made possible by funding from the Carl Zeiss Stiftung. ÁS acknowledges funding from the European Research Council (ERC) under the European Union’s Horizon 2020 research and innovation programme (grant agreement No. 101117455).

## DATA AVAILABILITY

All code to reproduce the analysis and figures can be publicly accessed via [https://github.com/svenbuder/golden\\_thread\\_I](https://github.com/svenbuder/golden_thread_I). The used simulation snapshot can be publicly accessed as FITS file via [https://github.com/svenbuder/preparing\\_NIHAO](https://github.com/svenbuder/preparing_NIHAO). Original data, more snapshots and other galaxies can be found at [https://tobias-buck.de/#sim\\_data](https://tobias-buck.de/#sim_data). We encourage interested readers to get in contact with the authors for full data access and advice for use and cite Buck et al. (2020, 2021).

## SOFTWARE

PYTHON (version 3.12.11) and included its packages ASTROPY (v. 7.1.0; [Astropy Collaboration et al. 2013, 2018](#)), HYppo (v. 0.5.2; [Panda et al. 2019](#)), IPYTHON (v. 9.1.0; [Pérez & Granger 2007](#)), MATPLOTLIB (v. 3.10.3; [Hunter 2007](#)), NUMPY (v. 2.2.6; [Walt et al. 2011](#)), as well as SCIPY (v. 1.16.0; [Virtanen et al. 2020](#)); TOPCAT (version 4.7; [Taylor 2005](#));

## REFERENCES

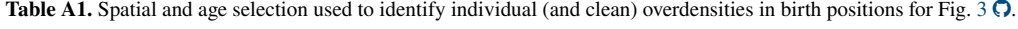
- Abdurro'uf et al., 2022, *ApJS*, **259**, 35  
 Aguado D. S., et al., 2021, *ApJ*, **908**, L8  
 Arentsen A., et al., 2020a, *MNRAS*, **491**, L11  
 Arentsen A., et al., 2020b, *MNRAS*, **496**, 4964  
 Asplund M., Grevesse N., Sauval A. J., Scott P., 2009, *ARA&A*, **47**, 481  
 Astropy Collaboration et al., 2013, *A&A*, **558**, A33  
 Astropy Collaboration et al., 2018, *AJ*, **156**, 123  
 Barbuy B., Chiappini C., Gerhard O., 2018, *ARA&A*, **56**, 223  
 Belokurov V., Kravtsov A., 2022, *MNRAS*, **514**, 689  
 Belokurov V., et al., 2006, *ApJ*, **642**, L137  
 Belokurov V., Erkal D., Evans N. W., Koposov S. E., Deason A. J., 2018, *MNRAS*, **478**, 611  
 Belokurov V., Sanders J. L., Fattah A., Smith M. C., Deason A. J., Evans N. W., Grand R. J. J., 2020, *MNRAS*, **494**, 3880  
 Bensby T., Feltzing S., Oey M. S., 2014, *A&A*, **562**, A71  
 Bensby T., et al., 2017, *A&A*, **605**, A89  
 Bensby T., et al., 2019, *The Messenger*, **175**, 35  
 Binney J., 2012, *MNRAS*, **426**, 1324  
 Bird J. C., Kazantzidis S., Weinberg D. H., Guedes J., Callegari S., Mayer L., Madau P., 2013, *ApJ*, **773**, 43  
 Bland-Hawthorn J., Gerhard O., 2016, *ARA&A*, **54**, 529  
 Brook C. B., Kawata D., Gibson B. K., Freeman K. C., 2004, *ApJ*, **612**, 894  
 Brown A. G. A., 2021, *ARA&A*, **59**, 59  
 Buck T., 2020, *MNRAS*, **491**, 5435  
 Buck T., Macciò A. V., Dutton A. A., Obreja A., Frings J., 2019, *MNRAS*, **483**, 1314  
 Buck T., Obreja A., Macciò A. V., Minchev I., Dutton A. A., Ostriker J. P., 2020, *MNRAS*, **491**, 3461  
 Buck T., Rybizki J., Buder S., Obreja A., Macciò A. V., Pfrommer C., Steinmetz M., Ness M., 2021, *MNRAS*, **508**, 3365  
 Buck T., Obreja A., Ratcliffe B., Lu Y., Minchev I., Macciò A. V., 2023, *MNRAS*, **523**, 1565  
 Buck T., Günes B., Viterbo G., Oliver W. H., Buder S., 2025, arXiv e-prints, p. [arXiv:2503.02456](#)  
 Buder S., et al., 2022, *MNRAS*, **510**, 2407  
 Buder S., Mijnarends L., Buck T., 2024, *MNRAS*, **532**, 1010  
 Buder S., Buck T., Chen Q.-H., Grasha K., 2025, *OJAp*, **8**, 47  
 Cameron A. J., Katz H., Rey M. P., Saxena A., 2023, *MNRAS*, **523**, 3516  
 Carrillo A., Deason A. J., Fattah A., Callingham T. M., Grand R. J. J., 2024, *MNRAS*, **527**, 2165  
 Carrillo A., Deason A. J., Fattah A., Grand R. J. J., Frakoudi F., 2025, arXiv e-prints, p. [arXiv:2509.24705](#)  
 Chabrier G., 2003, *PASP*, **115**, 763  
 Chiappini C., Matteucci F., Gratton R., 1997, *ApJ*, **477**, 765  
 Chiappini C., et al., 2019, *The Messenger*, **175**, 30  
 Chieff A., Limongi M., 2004, *ApJ*, **608**, 405  
 Conroy C., Naidu R. P., Zaritsky D., Bonaca A., Cargile P., Johnson B. D., Caldwell N., 2019, *ApJ*, **887**, 237  
 Da Costa G. S., et al., 2019, *MNRAS*, **489**, 5900  
 Das P., Hawkins K., Jofré P., 2020, *MNRAS*, **493**, 5195  
 Di Matteo P., Haywood M., Lehnert M. D., Katz D., Khoperskov S., Snaith O. N., Gómez A., Robichon N., 2019, *A&A*, **632**, A4  
 Dillamore A. M., Sanders J. L., 2025, *MNRAS*, **542**, 1331  
 Dodd E., Callingham T. M., Helmi A., Matsuno T., Ruiz-Lara T., Balbinot E., Lövdal S., 2023, *A&A*, **670**, L2  
 Ernestades H., Skúladóttir Á., Feltzing S., Feuillet D., 2025, arXiv e-prints, p. [arXiv:2509.06773](#)  
 Feuillet D. K., Frankel N., Lind K., Frinchaboy P. M., García-Hernández D. A., Lane R. R., Nitschelm C., Roman-Lopes A. r., 2019, *MNRAS*, **489**, 1742  
 Feuillet D. K., Feltzing S., Sahlholdt C. L., Casagrande L., 2020, *MNRAS*, **497**, 109  
 Feuillet D. K., Sahlholdt C. L., Feltzing S., Casagrande L., 2021, *MNRAS*, **508**, 1489  
 Freeman K., Bland-Hawthorn J., 2002, *ARA&A*, **40**, 487  
 Gaia Collaboration et al., 2016, *A&A*, **595**, A2  
 Gaia Collaboration et al., 2018, *A&A*, **616**, A1  
 Gallazzi A., Charlot S., Brinchmann J., White S. D. M., Tremonti C. A., 2005, *MNRAS*, **362**, 41  
 Gilmore G., Reid N., 1983, *MNRAS*, **202**, 1025  
 Grand R. J. J., et al., 2018, *MNRAS*, **474**, 3629  
 Gunes B., Buder S., Buck T., 2025, arXiv e-prints, p. [arXiv:2507.05060](#)  
 Hawkins K., Jofré P., Masseron T., Gilmore G., 2015, *MNRAS*, **453**, 758  
 Hayden M. R., et al., 2015, *ApJ*, **808**, 132  
 Haywood M., Di Matteo P., Lehnert M. D., Snaith O., Khoperskov S., Gómez A., 2018, *ApJ*, **863**, 113  
 Helmi A., 2020, *ARA&A*, **58**, 205  
 Helmi A., Babusiaux C., Koppelman H. H., Massari D., Veljanoski J., Brown A. G. A., 2018, *Nature*, **563**, 85  
 Horta D., et al., 2021, *MNRAS*, **500**, 1385  
 Hunter J. D., 2007, *Comput Sci Eng*, **9**, 90  
 Ji X., Belokurov V., Maiolino R., Monty S., Isobe Y., Kravtsov A., McClymont W., Übler H., 2025, arXiv e-prints, p. [arXiv:2505.12505](#)  
 Karakas A. I., Lugaro M., 2016, *ApJ*, **825**, 26  
 Katz D., et al., 2023, *A&A*, **674**, A5  
 Khoperskov S., Minchev I., Steinmetz M., Marabotto J., Kordopatis G., Delgado Gomez J., Libeskind N., 2023a, arXiv e-prints, p. [arXiv:2310.05287](#)  
 Khoperskov S., et al., 2023b, *A&A*, **677**, A90  
 Khoperskov S., et al., 2023c, *A&A*, **677**, A91  
 Kirby E. N., Cohen J. G., Guhathakurta P., Cheng L., Bullock J. S., Gallazzi A., 2013, *ApJ*, **779**, 102  
 Knollmann S. R., Knebe A., 2009, *ApJS*, **182**, 608  
 Koppelman H. H., Helmi A., Massari D., Price-Whelan A. M., Starkenburg T. K., 2019, *A&A*, **631**, L9  
 Kunder A., et al., 2025, *AJ*, **170**, 173  
 Lucey M., et al., 2019, *MNRAS*, **488**, 2283  
 Lucey M., et al., 2022, *MNRAS*, **509**, 122  
 Martin N. F., et al., 2024, *A&A*, **692**, A115  
 Matsuno T., Hirai Y., Tarumi Y., Hotokezaka K., Tanaka M., Helmi A., 2021, *A&A*, **650**, A110  
 Minchev I., Chiappini C., Martig M., 2013, *A&A*, **558**, A9  
 Monty S., et al., 2024, *MNRAS*, **533**, 2420  
 Mori A., Di Matteo P., Salvadori S., Khoperskov S., Pagnini G., Haywood M., 2024, *A&A*, **690**, A136  
 Myeong G. C., Evans N. W., Belokurov V., Amorisco N. C., Koposov S. E., 2018, *MNRAS*, **475**, 1537  
 Myeong G. C., Vasiliev E., Iorio G., Evans N. W., Belokurov V., 2019, *MNRAS*, **488**, 1235  
 Naidu R. P., Conroy C., Bonaca A., Johnson B. D., Ting Y.-S., Caldwell N., Zaritsky D., Cargile P. A., 2020, *ApJ*, **901**, 48  
 Naidu R. P., et al., 2021, *ApJ*, **923**, 92  
 Naidu R. P., et al., 2022a, arXiv e-prints, p. [arXiv:2204.09057](#)  
 Naidu R. P., et al., 2022b, *ApJ*, **926**, L36  
 Ness M., et al., 2013a, *MNRAS*, **430**, 836  
 Ness M., et al., 2013b, *MNRAS*, **432**, 2092  
 Nissen P. E., Schuster W. J., 2010, *A&A*, **511**, L10  
 Nissen P. E., Amarsi A. M., Skúladóttir Á., Schuster W. J., 2024, *A&A*, **682**, A116  
 Obreja A., Buck T., Macciò A. V., 2022, *A&A*, **657**, A15  
 Orkney M. D. A., Laporte C. F. P., Grand R. J. J., Springel V., 2025, arXiv e-prints, p. [arXiv:2506.07038](#)  
 Ou X., Ji A. P., Frebel A., Naidu R. P., Limberg G., 2024, *ApJ*, **974**, 232

- Panda S., Palaniappan S., Xiong J., Bridgeford E. W., Mehta R., Shen C., Vogelstein J. T., 2019, arXiv e-prints, p. arXiv:1907.02088
- Pérez F., Granger B. E., 2007, *Comput Sci Eng*, 9, 21
- Planck Collaboration et al., 2014, *A&A*, 571, A16
- Pontzen A., Roškar R., Stinson G. S., Woods R., 2013, pynbody: Astrophysics Simulation Analysis for Python, Astrophysics Source Code Library, record ascl:1305.002
- Portail M., Wegg C., Gerhard O., Ness M., 2017, *MNRAS*, 470, 1233
- Queiroz A. B. A., et al., 2023, *A&A*, 673, A155
- Ratcliffe B. L., Ness M. K., Buck T., Johnston K. V., Sen B., Beraldo e Silva L., Debattista V. P., 2022, *ApJ*, 924, 60
- Ratcliffe B., et al., 2025, *A&A*, 698, A267
- Rybicki J., Just A., Rix H.-W., 2017, *A&A*, 605, A59
- Sanders J. L., Binney J., 2015, *MNRAS*, 447, 2479
- Santana F. A., et al., 2021, *AJ*, 162, 303
- Schönrich R., Binney J., 2009, *MNRAS*, 399, 1145
- Seitenzahl I. R., et al., 2013, *MNRAS*, 429, 1156
- Senchyna P., Plat A., Stark D. P., Rudie G. C., Berg D., Charlot S., James B. L., Mingozi M., 2024, *ApJ*, 966, 92
- Sestito F., et al., 2021, *MNRAS*, 500, 3750
- Sharma S., Hayden M. R., Bland-Hawthorn J., 2021, *MNRAS*, 507, 5882
- Skúladóttir Á., Ernandes H., Feuillet D. K., Mori A., Feltzing S., Lucchesi R. E. R., Di Matteo P., 2025, *ApJ*, 986, L21
- Snaith O., Haywood M., Di Matteo P., Lehnert M. D., Combes F., Katz D., Gómez A., 2015, *A&A*, 578, A87
- Soderblom D. R., 2010, *ARA&A*, 48, 581
- Spitoni E., Silva Aguirre V., Matteucci F., Calura F., Grisoni V., 2019, *A&A*, 623, A60
- Starkenburg E., et al., 2017, *MNRAS*, 471, 2587
- Stinson G., Seth A., Katz N., Wadsley J., Governato F., Quinn T., 2006, *MNRAS*, 373, 1074
- Stinson G. S., Brook C., Macciò A. V., Wadsley J., Quinn T. R., Couchman H. M. P., 2013, *MNRAS*, 428, 129
- Taylor M. B., 2005, *ASPC*, 347, 29
- Thomas G. F., Battaglia G., Grand R. J. J., Aguiar Álvarez A., 2025, arXiv e-prints, p. arXiv:2504.10398
- Trick W. H., Coronado J., Rix H.-W., 2019, *MNRAS*, 484, 3291
- Vasiliev E., 2019, *MNRAS*, 482, 1525
- Virтанен P., et al., 2020, *Nature Methods*, 17, 261
- Wadsley J. W., Keller B. W., Quinn T. R., 2017, *MNRAS*, 471, 2357
- Walt S. v. d., Colbert S. C., Varoquaux G., 2011, *Comput Sci Eng*, 13, 22
- Wang L., Dutton A. A., Stinson G. S., Macciò A. V., Penzo C., Kang X., Keller B. W., Wadsley J., 2015, *MNRAS*, 454, 83
- Yoshii Y., 1982, *PASJ*, 34, 365
- Yuan Z., et al., 2020, *ApJ*, 891, 39
- da Silva A. R., Smiljanic R., 2023, *A&A*, 677, A74

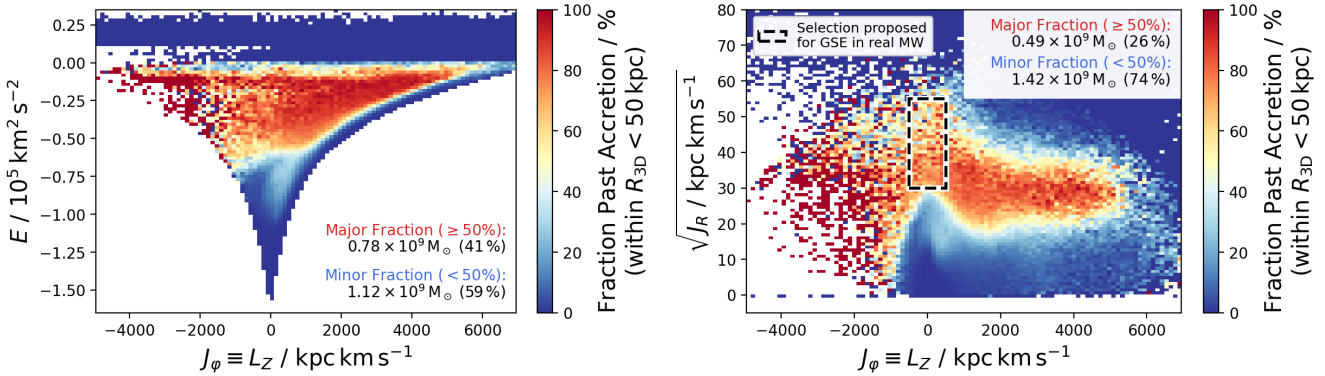
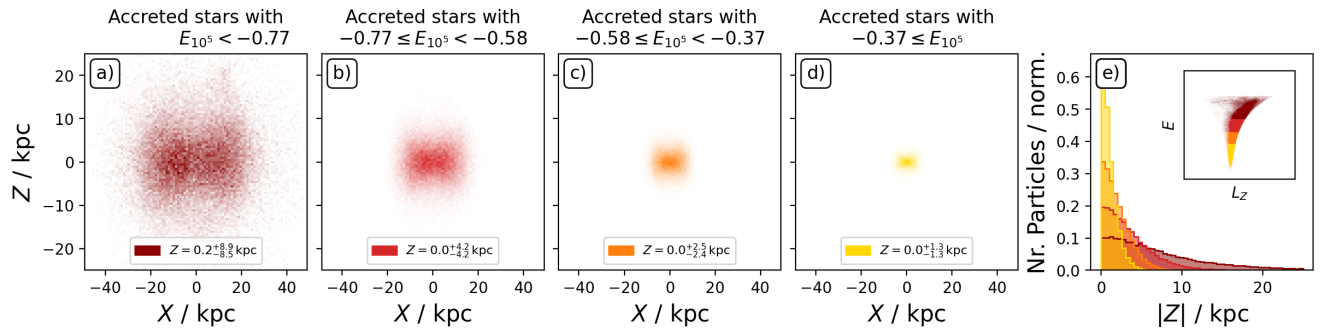
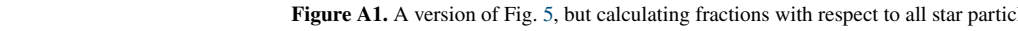
Zn. We omit He, as it scales linearly with [Fe/H]. We note that Khoperskov et al. (2023c, see their Fig. 15) found significantly different trends of sub-Solar [C/Fe] and sub-Solar [N/Fe] increasing towards Solar values at Solar [Fe/H].

## APPENDIX A: ADDITIONAL INFORMATION

- (i) We provide both the initial selection and resulting average spatial and age ranges of the major accreted structure in Tab. A1.
- (ii) Fig. A1 shows the same distribution of stars in bins of  $L_Z$  vs.  $E$  and  $L_Z$  vs.  $\sqrt{J_R}$  as Fig. 5. In this version, we include ongoing accretion in addition to past accretion and in-situ formation when calculating the fractional contribution for each bin.
- (iii) Fig. A2 shows the spatial distribution of accreted stars as Fig. 8, but for the  $X - Z$  direction.
- (iv) Fig. A3 includes the chemical distribution of accreted stars beyond the ones already shown in Fig. 7. They include the alpha-process elements O, Ne, Si, and S (behaving like the alpha-process element Mg), the odd-Z elements Na, Cl, and Cu (behaving like the odd-Z element Al), the iron-peak element Mn (behaving like the iron-peak element Ni), the neutron-capture elements Y, Ce, and Eu (behaving like the neutron-capture element Ba). For completeness, we also include C, N, Ti, and

**Table A1.** Spatial and age selection used to identify individual (and clean) overdensities in birth positions for Fig. 3 

Property	X Range	Y Range	Z Range	Age Range	X Center	Y Center	Z Center	Median Age	Median [Fe/H]
Unit	kpc	kpc	kpc	Gyr	kpc	kpc	kpc	Gyr	dex
1	-40..-25	10..33	-175..-155	11.0..13.0	-32	20	-166	$12.24 \pm 0.03$	$-1.50 \pm 0.18$
2	-19..-9	46..68	-174..-160	10.9..12.9	-13	56	-166	$11.92 \pm 0.03$	$-1.27 \pm 0.12$
3	0..12	20..45	-176..-164	10.8..12.8	6	32	-169	$11.79 \pm 0.03$	$-1.21 \pm 0.17$
4	-53..-38	30..60	-166..-144	10.7..12.7	-43	39	-160	$11.72 \pm 0.04$	$-1.36 \pm 0.24$
5	-80..-65	32..52	-154..-130	10.6..12.6	-73	39	-143	$11.60 \pm 0.04$	$-1.17 \pm 0.15$
6	-79..-72	50..66	-142..-124	10.5..12.5	-75	60	-132	$11.48 \pm 0.04$	$-1.12 \pm 0.16$
7	-86..-79	50..75	-132..-114	10.4..12.4	-83	61	-121	$11.37 \pm 0.04$	$-1.14 \pm 0.17$
8	-92..-80	65..90	-115..-98	10.3..12.3	-87	74	-106	$11.29 \pm 0.03$	$-1.12 \pm 0.18$
9	-114..-106	64..81	-86..-72	10.2..12.2	-109	70	-80	$11.16 \pm 0.03$	$-0.99 \pm 0.20$
10	-120..-107	45..64	-86..-66	10.1..12.1	-113	54	-75	$11.06 \pm 0.04$	$-1.04 \pm 0.15$
11	-117..-112	39..51	-71..-62	9.9..11.9	-115	46	-67	$10.96 \pm 0.03$	$-0.92 \pm 0.14$
12	-120..-100	29..46	-62..-44	9.8..11.8	-116	36	-52	$10.82 \pm 0.07$	$-0.98 \pm 0.12$
13	-113..-103	14..30	-61..-43	9.7..11.7	-108	23	-50	$10.62 \pm 0.04$	$-0.98 \pm 0.12$
14	-104..-98	8..25	-50..-43	9.5..11.5	-102	14	-49	$10.51 \pm 0.04$	$-0.92 \pm 0.10$
15	-93..-84	12..32	-66..-48	9.4..11.4	-88	23	-57	$10.42 \pm 0.03$	$-0.94 \pm 0.10$
16	-82..-73	11..29	-63..-49	9.3..11.3	-78	18	-58	$10.31 \pm 0.03$	$-0.90 \pm 0.09$
17	-62..-53	9..34	-69..-54	9.2..11.2	-57	25	-62	$10.19 \pm 0.04$	$-0.83 \pm 0.08$
18	-36..-20	17..33	-73..-44	9.1..11.1	-33	25	-63	$10.09 \pm 0.04$	$-0.79 \pm 0.10$
19	-36..-20	-10..15	-73..-44	9.0..11.0	-32	4	-54	$9.98 \pm 0.04$	$-0.86 \pm 0.06$
20	-31..-19	-25..-5	-43..-28	8.9..10.9	-24	-14	-36	$9.88 \pm 0.04$	$-0.74 \pm 0.09$
21	-12..0	-35..-15	-23..-6	8.8..10.8	-6	-26	-15	$9.75 \pm 0.02$	$-0.81 \pm 0.07$
22	9..19	-34..-12	2..16	8.6..10.6	14	-17	7	$9.61 \pm 0.43$	$-0.66 \pm 0.12$
23	20..35	-6..10	14..34	8.5..10.5	26	2	23	$9.56 \pm 0.02$	$-0.77 \pm 0.06$
24	14..28	19..28	25..36	8.4..10.4	24	24	30	$9.46 \pm 0.03$	$-0.72 \pm 0.05$
25	10..20	27..41	23..38	8.3..10.3	16	34	29	$9.34 \pm 0.03$	$-0.70 \pm 0.05$
26	6..15	31..41	15..27	8.2..10.2	10	37	22	$9.22 \pm 0.02$	$-0.68 \pm 0.05$
27	-4..15	28..39	8..17	8.1..10.1	-1	34	14	$9.10 \pm 0.04$	$-0.64 \pm 0.05$
28	-17..-3	12..29	-8..7	8.0..10.0	-8	23	-1	$9.04 \pm 0.03$	$-0.65 \pm 0.04$
29	-19..-5	-13..-1	-12..0	7.9..9.9	-7	-4	-6	$8.89 \pm 0.04$	$-0.60 \pm 0.08$
30	-21..-16	-21..-10	3..10	7.8..9.8	8	-15	8	$8.80 \pm 0.03$	$-0.57 \pm 0.06$
31	3..27	-6..-3	2..11	7.7..9.7	11	-1	5	$8.70 \pm 0.03$	$-0.50 \pm 0.03$
32	-23..-19	-16..-13	-4..-5	7.6..9.6	-5	-2	0	$8.62 \pm 0.36$	$-0.49 \pm 0.07$

**Figure A1.** A version of Fig. 5, but calculating fractions with respect to all star particles **Figure A2.** Same as Fig. 8, but for  $X$ - $Z$  dimensions 

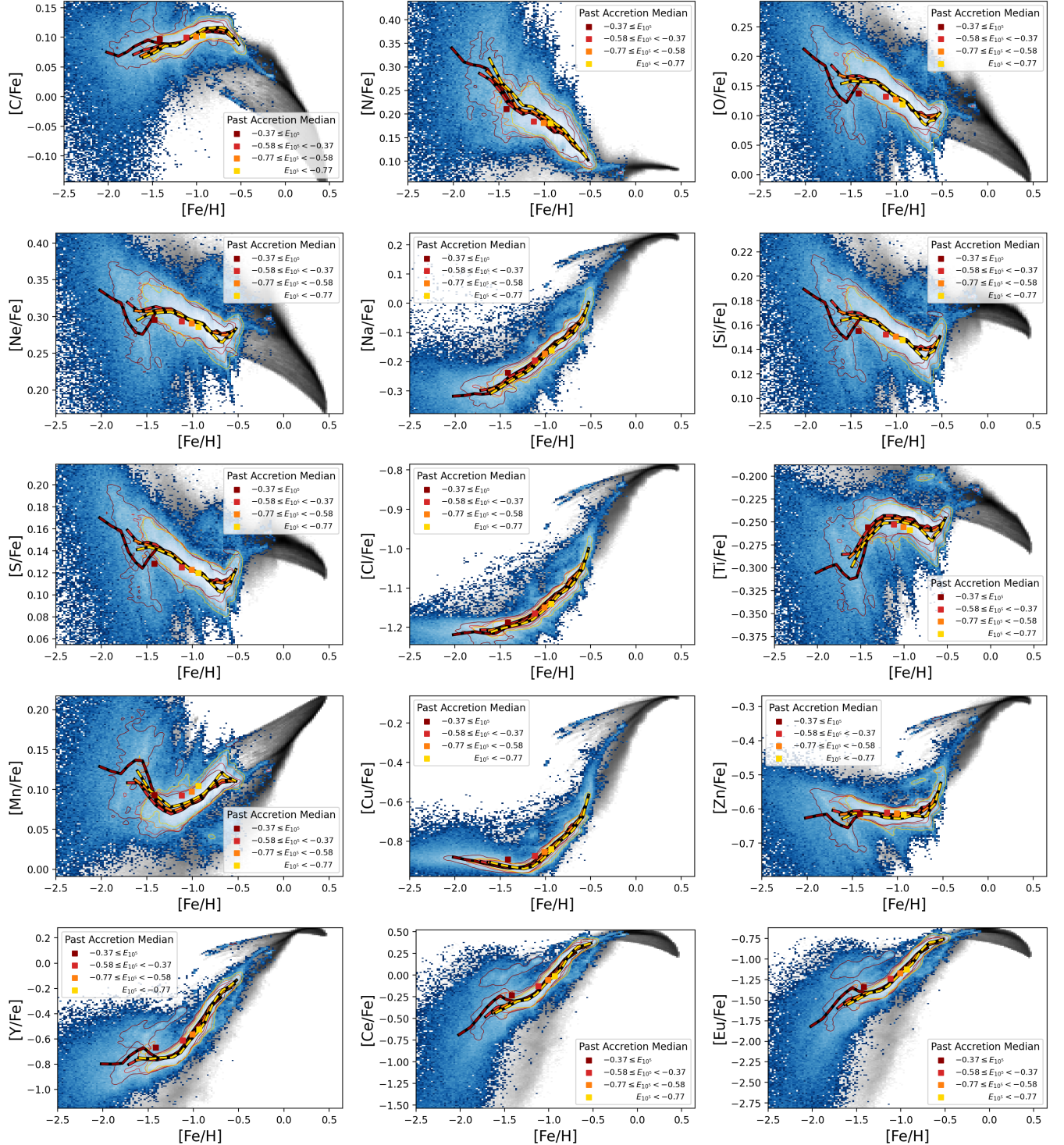


Figure A3. Same as Fig. 7, for C, N, O, Ne, Na, Si, S, Cl, Ti, Mn, Cu, Zn, Y, Ce, and Eu in the others